Chemical Engineering Journal 509 (2025) 161095

Contents lists available at ScienceDirect

Chemical Engineering Journal

journal homepage: www.elsevier.com/locate/cej

One-pot synthesis of hierarchical assembly of $NiMoO_4/MoS_2/Ni_3S_2$ on nickel foam for highly efficient and durable electrocatalytic hydrogen evolution reaction in a wide pH range

Senkai Han [a], Huiqin Yao [b], Jiayi Zhan [a,1], Chaonan Wang [a], Siqi Zhang [a], Qingyang Gu [c,*], Cheng Li [d,*], Shenghan Zhang [e], Hongliang Dong [e,f,*], Shulan Ma [a,*]

[a] Beijing Key Laboratory of Energy Conversion and Storage Materials and College of Chemistry, Beijing Normal University, Beijing 100875, China
[b] School of Basic Medical Sciences, Ningxia Medical University, Yinchuan 750004, China
[c] College of New Materials and Chemical Engineering, Beijing Institute of Petrochemical Technology, Beijing 102617, China
[d] Shanghai Institute of Applied Physics, Chinese Academy of Sciences, Shanghai 201800, China
[e] Center for High Pressure Science and Technology Advanced Research, Shanghai 201203, China
[f] Shanghai Key Laboratory of Material Frontiers Research in Extreme Environments (MFree), Shanghai Advanced Research in Physical Sciences (SHARPS), Pudong, Shanghai 201203, China

ARTICLE INFO

Keywords:
$NiMoO_4$
MoS_2
Heterojunction
Electrocatalytic water splitting
Hydrogen evolution reaction

ABSTRACT

Development of cost-effective, durable and pH-universal electrocatalysts toward hydrogen evolution reaction (HER) is of great significant for large scale hydrogen energy production. Here, via a one-pot hydrothermal reaction, the hierarchical assemblies of $NiMoO_4/MoS_2/Ni_3S_2$/NF-*n* (NF is nickel foam, and *n* represents S/Mo molar ratios of 1.3, 1.7, and 2.0) are facilely fabricated. The low reaction temperature (< 160 °C) and low S/Mo ratios (≤ 2) ensure the formation of low crystalline MoS_2 and amorphous $NiMoO_4$ phases. The optimized $NiMoO_4/MoS_2/Ni_3S_2$/NF-1.7 exhibits outstanding HER performance, requiring ultra-low overpotentials of 72, 49, and 166 mV to achieve the current density of 10 $mA{\cdot}cm^{-2}$ under acidic, alkaline, and neutral conditions, respectively. Also, extremely high durability (stability time ≥ 200 h) is achieved in both alkaline and neutral electrolytes. X-ray absorption fine structures (XAFS) determine the average valence of Mo is +4.27, proving the co-existence of the two phases of MoS_2 and $NiMoO_4$. Density functional theory (DFT) calculations reveal the $NiMoO_4$ plays a predominant role in facilitating HER activity. In acidic solution, the O atom of $NiMoO_4$ with the lowest Gibbs free energy of hydrogen adsorption (ΔG_{H^*}) of 0.16 eV works as the active site for HER; in alkaline condition, Ni atom of $NiMoO_4$ with much low Gibbs free energy of water dissociation (ΔG_{H2O^*}) of 0.68 eV serves as the active site for water adsorption/dissociation. This work presents a novel perspective to electrocatalyst exploration by incorporating low crystalline and amorphous transitional metal sulfides/oxides, achieving superb HER performance to realize large-scale hydrogen production in a wide pH range.

1. Introduction

The advancement of modern society hinges critically on the acquisition of sustainable and eco-friendly energy sources. Hydrogen (H_2) is an ideal carrier on account of the exceptional energy density, zero carbon emission, and renewability. Presently, the majority of hydrogen is derived from coal gasification or steam-methane reforming, leading to greenhouse gas emissions that violate to the environmental protection [1,2]. In contrast, electrochemical water splitting is a promising strategy for producing highly pure H_2 [3,4], while the hydrogen evolution reaction (HER) on cathode generally requires a large overpotential due to the electrode-reaction barrier [5] and Ohmic loss [6]. To overcome the energetic barriers in HER and enhance electrolytic efficiency, electrocatalysts are commonly employed to reduce the overpotentials. Platinum (Pt)-based catalysts are deemed to be the state-of-the-art ones for HER, while their scarcity and high price limit the practical application [7]. It is imperative to investigate cost-effective non-noble metal electrocatalysts. Also, the electrocatalysts capable of operating over a wide

* Corresponding authors.
E-mail addresses: guqingyang@bipt.edu.cn (Q. Gu), licheng@sinap.ac.cn (C. Li), hongliang.dong@hpstar.ac.cn (H. Dong), mashulan@bnu.edu.cn (S. Ma).
[1] Present address: The British School of Beijing, Shunyi, Beijing 101300, China.

https://doi.org/10.1016/j.cej.2025.161095
Received 17 December 2024; Received in revised form 11 February 2025; Accepted 26 February 2025
Available online 1 March 2025

pH range can expand the applicability. Therefore, development of pH-universal electrocatalysts for HER is of great significance [8].

Transition metal sulfides (TMSs) are considered to be potential substitutes for noble-metal catalysts due to their exceptional electrical conductivity and catalytic activity [9,10]. Nickel sulfides have emerged as promising electrocatalysts for water splitting [11]. Ni_3S_2, as one kind of nickel sulfide, has good electrical conductivity, due to its including zero-valent Ni and triangular Ni-Ni networks [12]. Besides, the Ni-S bonds of Ni_3S_2 exhibit high chemical reactivity towards hydrogen, thereby conducing the HER activity [13]. However, insufficient active sites and poor stability in aqueous media impede its widespread application [14]. In situ growing Ni_3S_2-based materials on certain substrate is an effective strategy to boost the stability. Nickel foam (NF) with a three-dimensional (3D) framework can not only serve as a conductive substrate for constructing self-supported electrodes, but also provide nickel source to synthesize Ni_3S_2-based catalysts with acceptable HER performance [15–17]. MoS_2 is a layered metal sulfide with multiple S-Mo-S sandwich layers held together by weak intermolecular force [18,19]. Density functional theory (DFT) calculations and experiments confirmed the edge S sites of MoS_2 had high sorption capability for hydrogen [20]. However, limited active sites, inert basal planes, and weak conductivity of MoS_2 impede the catalytic performance [21,22]. In addition, electron transfer at heterogeneous interfaces may modulate electronic structure, benefiting to enhancement of intrinsic activity. As reported, the MoS_2/Ni_3S_2 composite interacted with MoS_2 nanosheets on Ni_3S_2 nanorods exhibited good HER performance, showing a 98 mV overpotential at the current density of 10 mA·cm^{-2} (η_{10} = 98 mV) in 1 M KOH [23]. The interfacial interactions between MoS_2 and Ni_3S_2 favored the chemisorption of H-intermediates. Therefore, effective integration of the MoS_2 with Ni_3S_2 is expected to bring superior performance.

Recently, transition metal oxides (TMOs) have attracted increasing attention in the field of water electrolysis to produce H_2 [24,25]. However, the limited conductivity and catalytic activity of TMOs constrain the practical application [26]. Nickel molybdate ($NiMoO_4$) is a typical binary metal oxide that possesses abundant active sites, robust structures, and favorable water dissociation ability [27,28]. In $NiMoO_4$, Ni atoms normally serve as water dissociation centers, while O sites facilitate H_2 generation during HER [29]. Additionally, the augmented HER activity and kinetics of $NiMoO_4$ are primarily ascribed to the effective synergy between the species of Ni and Mo, along with the strong electronic interactions among the atoms [30]. The $NiMoO_4$ could be synthesized under a hydrothermal reaction of $Ni(NO_3)_2{\cdot}6H_2O$ with $Na_2MoO_4{\cdot}2H_2O$ [31,32] or $(NH_4)_6Mo_7O_{24}{\cdot}4H_2O$ [33–35]. The nanorod clusters of NF/$NiMoO_4$@HeBiMoNi exhibited optimal HER activity (η_{10} = 53 mV) in 1 M KOH [33]. As known, amorphous materials have atomic-scale flexibility and abundant structural defects, achieving maximal exposure of active sites [36,37]. Zhang et al. [38] reported a sandwich-structured electrocatalyst composed of amorphous Ni_2P/crystalline P-$NiMoO_4$/amorphous P-$NiMoO_4$, showing an ultra-low η_{10} of 45 mV for HER in alkaline media. The good performance was interpreted as interfacial effects of the contained phases leading to tunable electronic structures.

The reported $NiMoO_4$ presented acceptable HER performance only in alkaline environment, with less desirable activity and stability in acidic and neutral electrolytes. It is necessary to explore $NiMoO_4$-involving composites showing preferable HER activity in a wide pH range. Through hydrothermal reaction, deposition and phosphating treatment, Feng et al. [39] prepared C-Co_2P@P-$NiMoO_4$/NF, which exhibited good HER performance in alkaline, acidic, and neutral media with η_{10} of 59, 37, and 50 mV, respectively. However, the complex synthesis procedures hindered industrial promotion. Given the remarkable electrocatalytic performance of MoS_2/Ni_3S_2 mentioned above, we want ot know what would happen if the $NiMoO_4$ integrates with the MoS_2 and Ni_3S_2.

In this work, using NF as the substrate and Ni source, via a one-pot hydrothermal reaction of $Na_2MoO_4{\cdot}2H_2O$ with thioacetamide (CH_3CSNH_2) at 160 °C and S/Mo ratios ≤ 2, the hierarchical composites of $NiMoO_4$/MoS_2/Ni_3S_2/NF-*n* (*n* represents the molar ratios of S/Mo as 1.3, 1.7, and 2.0) are facilely assembled. The low reaction temperature and smaller S dosage (relative to Mo) lead to the formation of low crystalline MoS_2 and $NiMoO_4$. Featuring the morphology of nanosheets dispersed on microspheres to expose more active sites, the optimized sample of $NiMoO_4$/MoS_2/Ni_3S_2/NF-1.7 demonstrates wonderful HER performance and remarkable stability under pH-universal conditions. The ultra-low η_{10} of 72, 49, and 166 mV, coupled with the long-term stability time ≥ 38, 200, and 200 h under acidic, alkaline, and neutral conditions, respectively, indicating the first-rate electrocatalytic performance. X-ray absorption fine structure (XAFS) of $NiMoO_4$/MoS_2/Ni_3S_2/NF-1.7 reveals an average Mo valence of +4.27, suggesting co-existence of the two Mo-containing phases of $NiMoO_4$ and MoS_2. DFT calculations confirm that in $NiMoO_4$/MoS_2/Ni_3S_2 heterojunction, the $NiMoO_4$ makes a dominant contribution to promoting HER activity in both acidic and alkaline electrolytes, especially to the important step of water dissociation in alkaline media. The synergistic interactions between $NiMoO_4$ and MoS_2 significantly reduce the Gibbs free energy of water dissociation (ΔG_{H2O^*}) and hydrogen adsorption ($|\Delta G_{H^*}|$) of the catalysts. Total density of state (TDOS) demonstrates the hetero-interfaces increase the carrier density of the catalysts, elevating the electrical conductivity. This work provides a significant reference for tailoring new kinds of hybrid materials applied in large-scale hydrogen production in a wide pH range.

2. Experimental section

2.1. Preparation of composites of $NiMoO_4$/MoS_2/Ni_3S_2/NF-*n* and control samples of Ni_3S_2/NF and $NiMoO_4$/NF

A series of $NiMoO_4$/MoS_2/Ni_3S_2/NF-*n* materials were synthetized via a simple one-pot hydrothermal reaction. The amount of $Na_2MoO_4{\cdot}2H_2O$ was fixed at 1.2 mmol (289.2 mg), while the dosages of CH_3CSNH_2 varied from 1.5 mmol (112.7 mg) to 2.0 mmol (150.3 mg), and to 2.4 mmol (180.4 mg), corresponding to S/Mo molar ratios of 1.3, 1.7, and 2.0, respectively. The solids were dissolved in deionized water (30 mL) with stirring for 20 min. A piece of NF was then placed into the resulting solutions and subjected to a 24 h reaction at 160 °C in a Teflon-lined autoclave (50 mL). After naturally cooling, the products of $NiMoO_4$/MoS_2/Ni_3S_2/NF-*n* (*n* = 1.3, 1.7, and 2.0) were rinsed using ethanol and water, followed by vacuum drying.

The control sample of $NiMoO_4$/NF was synthesized via a similar process as the composites, except only adding Mo source of $Na_2MoO_4{\cdot}2H_2O$ (1.2 mmol) into the NF-immerged solution. The Ni_3S_2/NF was synthesized via the addition of only S source of CH_3CSNH_2 (2.0 mmol).

Table S1 lists the dosages of the reactants and average mass loadings on NF. Details of starting materials and characterization techniques are described in Supplementary Data.

2.2. DFT calculations

DFT was employed to theoretically assess the catalytic properties of the materials and identify the genuine catalytic active sites. The calculations were conducted within the framework of the all-electron projector augmented wave (PAW) method [40], as implemented in the Vienna *Ab initio* simulation package (VASP) code [41]. Perdew-Burke-Ernzerhof (PBE) function under the theory of generalized gradient approximation (GGA) was adopted to simulate the electron–ion interactions [42]. The Brillouin zones were sampled using a *k*-point mesh of 2 × 2 × 1 for surface calculations, while a denser *k*-point mesh of 3 × 3 × 3 was applied for density of states (DOS) calculations. Under a plane-wave cutoff energy of 400 eV, the self-consistent-field (SCF) calculations achieved the required accuracy when the force on atoms was < 0.01 eV/Å and the total energy difference between two consecutive iterations

was $< 10^{-5}$ eV [43]. The Supplementary Data provides the calculated formulas for ΔG_{H2O*} and ΔG_{H*}.

3. Results and discussion

3.1. Characterizations of $NiMoO_4/MoS_2/Ni_3S_2$/NF-n and control samples of Ni_3S_2/NF and $NiMoO_4$/NF

The $NiMoO_4/MoS_2/Ni_3S_2$/NF materials are prepared by a one-pot hydrothermal reaction (Scheme 1). The formation of the three phases of $NiMoO_4$, MoS_2, and Ni_3S_2 may follow the reactions below:

$$CH_3CSNH_2 + 3OH^- \rightarrow CH_3COO^- + NH_3 + S^{2-} + H_2O \quad (1)$$

$$3Ni + 2S^{2-} + 2H_2O + O_2 \rightarrow Ni_3S_2 + 4OH^- \quad (2)$$

$$Ni + 2S^{2-} + 2MoO_4^{2-} + 4H_2O \rightarrow MoS_2 + NiMoO_4 + 8OH^- \quad (3)$$

As shown in **Reaction 1**, due to the basicity of the reaction solution (pH ~ 8.5), the CH_3CSNH_2 undergoes hydrolysis to generate the S^{2-}, which works as the sulfur source. NF serves as both the Ni source to react with S^{2-}, leading to the formation of the Ni_3S_2 (**Reaction 2**). Simultaneously, metallic Ni reduces partial Mo(VI) of MoO_4^{2-} to Mo(IV) which binds to the S^{2-} to form MoS_2. Then, the remaining MoO_4^{2-} ions combine with Ni^{2+} (oxidized product of Ni^0) to yield the $NiMoO_4$ (**Reaction 3**).

X-ray diffractions (XRD) were measured to estimate the constituents of $NiMoO_4/MoS_2/Ni_3S_2$/NF-*n* and the control samples of Ni_3S_2/NF and $NiMoO_4$/NF (Fig. 1A). For Ni_3S_2/NF (Fig. 1A-a), the diffraction peaks at 2θ of 21.7°, 31.1°, 37.8°, 50.1°, and 55.3° respectively match with the planes (101), (110), (003), (211), and (300) of the Ni_3S_2 phase (JCPDS No. 44–1418) [16], and the observed ones at 44.5°, 51.8°, and 76.4° are related to the Ni^0 (JCPDS No. 04–0850) [44], in good agreement with those reported Ni_3S_2/NF [15,16,45–47]. The as-prepared $NiMoO_4$/NF (Fig. 1A-b) just displays diffraction peaks belonging to Ni^0 (NF), implying the $NiMoO_4$ phase (if has) may exist in an amorphous state. For the composites of $NiMoO_4/MoS_2/Ni_3S_2$/NF-*n*, as depicted in Fig. 1A-c-e, apart from the diffractions of Ni_3S_2 and NF, there is no peak of either $NiMoO_4$ or MoS_2 observable. From this we infer that if the two phases are present, they will exist either in amorphous or low crystalline state. The presence of $NiMoO_4$ and MoS_2 would be confirmed in subsequent characterizations.

Here the formation of low crystalline MoS_2 may due to the especial synthetic condition. From literature, crystalline MoS_2 can be obtained via a hydrothermal reaction of thiourea (CH_4N_2S) and $Na_2MoO_4{\cdot}2H_2O$ (S:Mo molar ratio was 4) at 180 °C for 24 h [48]. The crystalline MoS_2 can also be synthesized by reacting CH_4N_2S and $Na_2MoO_4{\cdot}2H_2O$ with a smaller S/Mo molar ratio of 3.3 at the temperature of 200 °C for 12 h [49]. However, at a much lower S:Mo (CH_3CSNH_2:Na_2MoO_4 = 2) ratio while a still high temperature of 200 °C (10 h), the obtained MoS_x presented an amorphous state [50]. These suggest that high temperature (> 180 °C) and large S/Mo ratios (> 2) favor the formation of crystalline MoS_2, while low temperature (< 180 °C) and small S/Mo ratio (< 2) would prefer the generation of low crystalline or amorphous MoS_2. In this work, the relatively low temperature (160 °C) and smaller S/Mo ratios (≤2) lead to the generation of MoS_2 with low crystallinity. At the lower temperature, the decomposition rate of CH_3CSNH_2 would be slower, hindering full vulcanization of the MoO_4^{2-} species [23] and formation of crystalline MoS_2 [51]. Consequently, the remaining MoO_4^{2-} in solutions would combine with the Ni^{2+} (dissolved from NF) to create the insoluble $NiMoO_4$. Based on literature [31,32], crystalline $NiMoO_4$ on NF can be synthesized by adding external Ni source of $Ni(NO_3)_2{\cdot}6H_2O$. Here we get the amorphous $NiMoO_4$, which may result from the low concentration of Ni^{2+} (dissolved from NF) decreasing the reaction rate with MoO_4^{2-}. Thus, appropriate conditions (low temperature and small S/Mo ratios) facilitate the co-appearance of the $NiMoO_4$ phase and the low crystallinity of the MoS_2.

X-ray photoelectron spectroscopy (XPS) of $NiMoO_4/MoS_2/Ni_3S_2$/NF-1.7 and $NiMoO_4$/NF were detected to study the valence state and chemical environment of the elements. For $NiMoO_4/MoS_2/Ni_3S_2$/NF-1.7, XPS survey spectrum (Fig. S1) confirms existence of S, O, Ni, and Mo elements. For Mo 3d (see Fig. 1B_1), the energies of 232.4 and 229.0 eV respectively correspond to Mo $3d_{3/2}$ and Mo $3d_{5/2}$ of Mo^{4+}, in accordance with reported MoS_2 [52–54]. Besides, the energies of 235.3 and 232.2 eV are attributed to Mo $3d_{3/2}$ and Mo $3d_{5/2}$ of Mo^{6+}, respectively [55]. Here the +6 valent Mo suggests the presence of MoO_4^{2-} or MoS_4^{2-}. Based on literature [56–59], the binding energies of Mo^{VI} in MoO_4^{2-} are slightly higher than those in MoS_4^{2-}, due to the stronger Mo-O (than Mo-S) bonding leading to a higher oxidation state of Mo. For Ni 2p (Fig. 1B_2), the 874.0 and 856.0 eV are assigned to Ni^{2+} $2p_{1/2}$ and $2p_{3/2}$, respectively [54], while 870.2 and 852.8 eV are related to Ni^0 $2p_{1/2}$ and Ni^0 $2p_{3/2}$ [60], confirming the existence of Ni_3S_2 (the valence of one Ni atom is zero) and NF (Ni^0 metal). For S, as shown in Fig. 1B_3, two signals at 163.2 and 162.0 eV are correlated with S^{2-} $2p_{1/2}$ and S^{2-} $2p_{3/2}$ in Ni_3S_2 and MoS_2 [48,61,62]. Due to inevitable air oxidation of sample surface, the signal at 167.7 eV assigned to S-O bonding is observed. Regarding O 1 s (Fig. 1B_4), the binding energy of 532.1 eV belongs to surface-adsorbed H_2O and/or OH groups, while the energy of 531.1 eV corresponds to metal-O (Mo/Ni-O) bonding in $NiMoO_4$ [34]. For the $NiMoO_4$/NF synthesized without S source, XPS survey spectrum (Fig. S2a) confirms the presence of O, Ni and Mo. As shown in Fig. S2b,

Scheme 1. Schematic illustration of synthetic process of $NiMoO_4/MoS_2/Ni_3S_2$/NF.

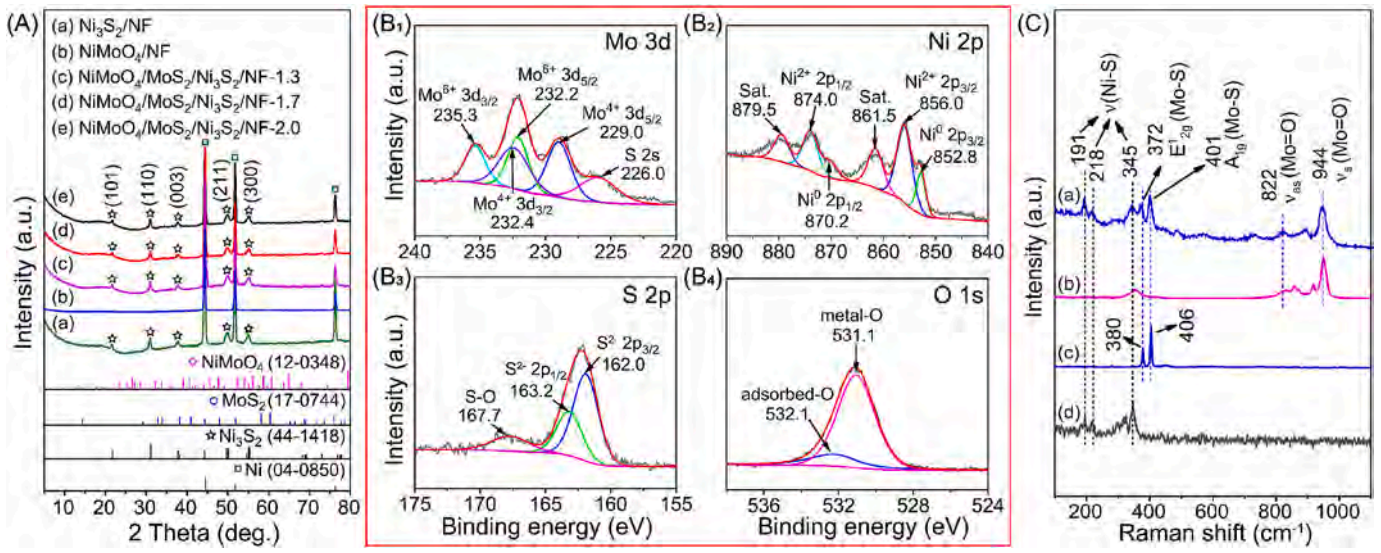

Fig. 1. (A) XRD patterns of (a) Ni_3S_2/NF, (b) $NiMoO_4$/NF, (c) $NiMoO_4/MoS_2/Ni_3S_2$/NF-1.3, (d) $NiMoO_4/MoS_2/Ni_3S_2$/NF-1.7, and (e) $NiMoO_4/MoS_2/Ni_3S_2$/NF-2.0; XPS spectra of $NiMoO_4/MoS_2/Ni_3S_2$/NF-1.7: (B_1) Mo 3d, (B_2) Ni 2p, (B_3) S 2p, and (B_4) O 1 s; (C) Raman spectra of (a) $NiMoO_4/MoS_2/Ni_3S_2$/F-1.7, (b) commercial $NiMoO_4$, (c) commercial MoS_2, and (d) Ni_3S_2/NF.

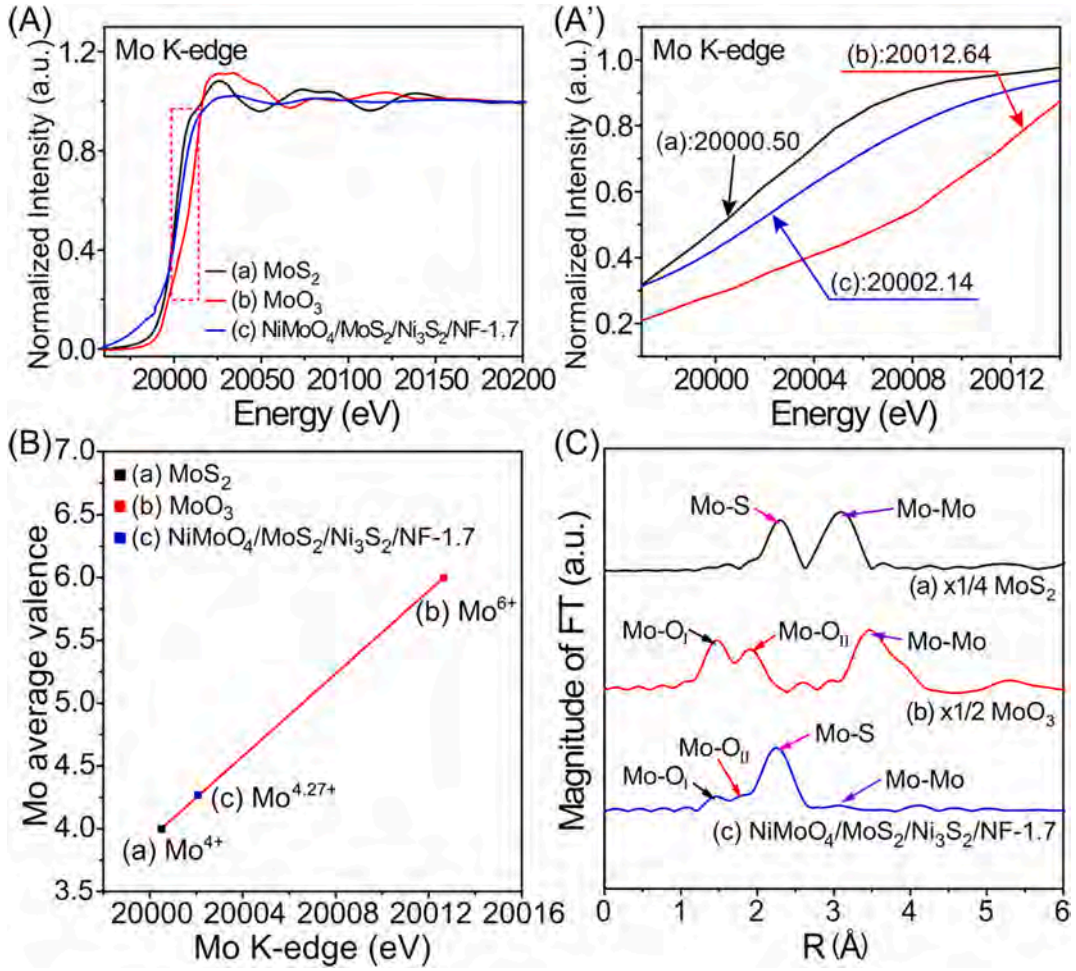

Fig. 2. (A, A') Mo K-edge XANES (A' is the enlarged view of the selected red square region in A), (B) average Mo valence obtained by linear fitting, and (C) Fourier transform (FT)-EXAFS of the (a) MoS_2, (b) MoO_3, and (c) $NiMoO_4/MoS_2/Ni_3S_2$/NF-1.7. (For interpretation of the references to colour in this figure legend, the reader is referred to the web version of this article.)

there only the binding energies of 235.4 and 232.3 eV ascribed to Mo $3d_{3/2}$ and Mo $3d_{5/2}$ of Mo^{VI} are observed, suggesting the presence of the only Mo^{VI}-based phase (here would be $NiMoO_4$). For Ni 2p (Fig. S2c), the 873.8 and 855.8 eV match well with Ni^{2+} $2p_{1/2}$ and Ni^{2+} $2p_{3/2}$, respectively, with satellite peaks at 879.5 and 861.6 eV. The O 1 s spectrum (Fig. S2d) indicates the 531.9 eV energy of adsorbed-O, while the 530.9 eV corresponds to Mo/Ni-O bonding. All these demonstrate the generation of the $NiMoO_4$ phase and no MoS_2 formed.

Raman spectra (Fig. 1C) were measured to investigate the bonding feature of the as-formed materials. In $NiMoO_4/MoS_2/Ni_3S_2$/NF-1.7 (Fig. 1C-a), vibration bands corresponding to Mo=O bonding are observed at 944 (symmetric mode) and 822 cm^{-1} (asymmetric mode) [34,63], consistent with those observed in commercial $NiMoO_4$ (Fig. 1C-b). From Fig. 1C-c, the commercial crystalline MoS_2 shows two typical bands at 406 and 380 cm^{-1} identified as out-of-plane A_{1g} and in-plane E^1_{2g} modes [14,64–66]. In $NiMoO_4/MoS_2/Ni_3S_2$/NF-1.7, there are two bands at 401 and 372 cm^{-1} observed, suggesting the MoS_2 phase has a certain crystallinity, though its XRD pattern shows no relevant diffractions. In Fig. 1C-a, the Raman shifts at 191, 218, and 345 cm^{-1} are attributed to Ni-S vibrations of the Ni_3S_2 phase [50], consistent with those found in Fig. 1C-d for Ni_3S_2/NF. All these results provide sufficient evidence for the formation of three phases of $NiMoO_4$, MoS_2, and Ni_3S_2 in the $NiMoO_4/MoS_2/Ni_3S_2$/NF.

To further explore the oxidation state of Mo and bonding characteristics in $NiMoO_4/MoS_2/Ni_3S_2$/NF-1.7, we investigated XANES of the sample. Mo K-edge XANES of MoS_2 (Mo^{4+}), MoO_3 (Mo^{6+}), and Mo^{4+}/Mo^{6+}-containing composite of $NiMoO_4/MoS_2/Ni_3S_2$/NF-1.7 are displayed in Fig. 2A, A'. The average valence of Mo can be inferred from the energy shift of XANES spectra. From Fig. 2A'-c, we see the energy (20002.14 eV) of Mo in $NiMoO_4/MoS_2/Ni_3S_2$/NF-1.7 is higher than pure

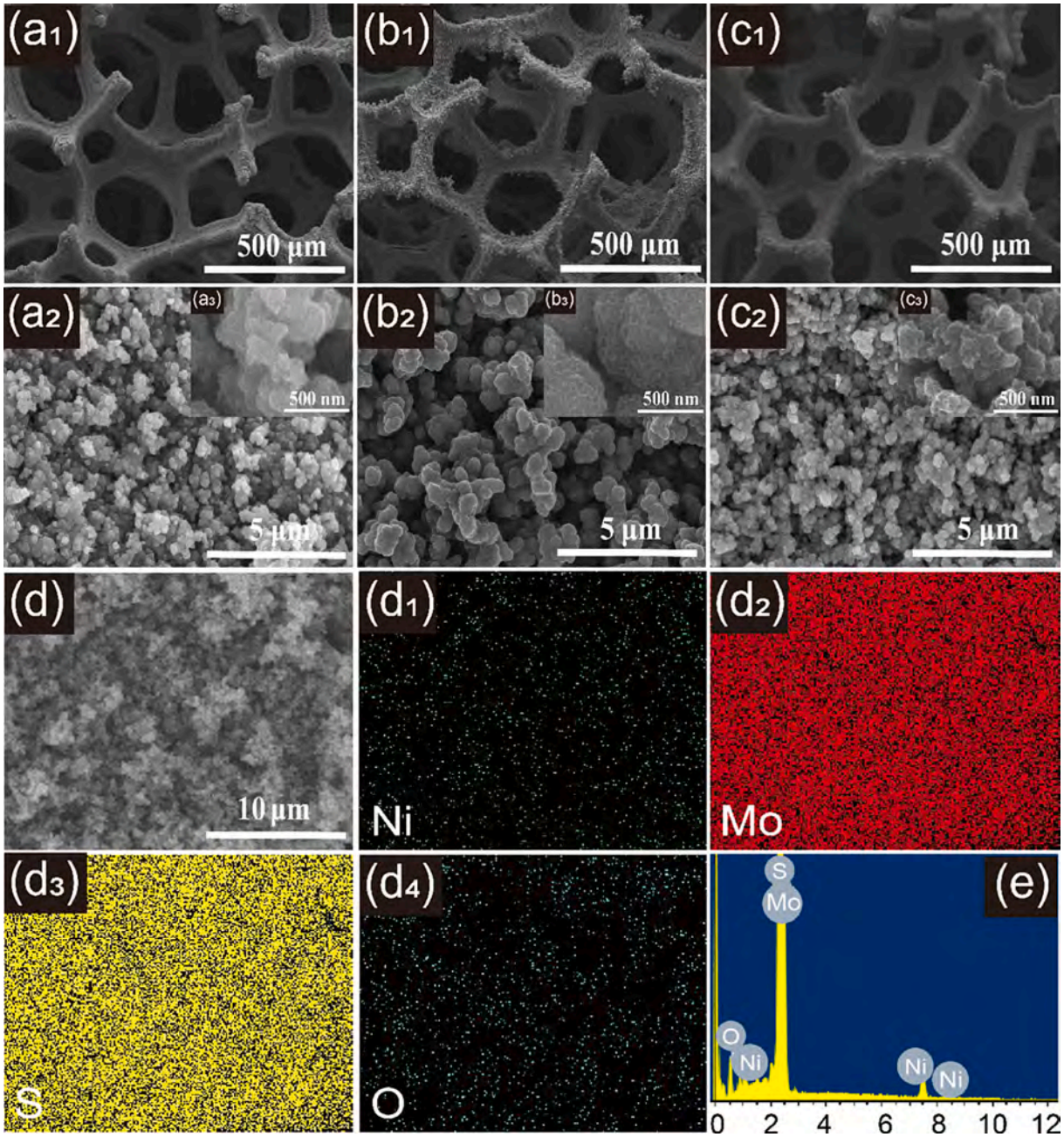

Fig. 3. SEM images of (a_1-a_3) $NiMoO_4/MoS_2/Ni_3S_2$/NF-1.3, (b_1-b_3, d) $NiMoO_4/MoS_2/Ni_3S_2$/NF-1.7, and (c_1-c_3) $NiMoO_4/MoS_2/Ni_3S_2$/NF-2.0; (d_1-d_4) elemental mapping in image (d) and (e) EDS spectrum of $NiMoO_4/MoS_2/Ni_3S_2$/NF-1.7.

MoS_2 (20000.50 eV, Fig. 2A'-a) but lower than MoO_3 (20012.64 eV, Fig. 2A'-b), suggesting that the average valence of Mo in $NiMoO_4/MoS_2/Ni_3S_2$/NF-1.7 is larger than +4 and lower than +6. From the linear analysis on valence state (see Fig. 2B), the average chemical valence of Mo is +4.27, indicating the co-existence of MoS_2 and $NiMoO_4$. Based on the average Mo valence calculations, the molar ratio of MoS_2 to $NiMoO_4$ may be determined to 6.41:1, indicating a significantly higher content of MoS_2 than $NiMoO_4$. Through extended X-ray absorption fine structure (EXAFS), the coordination motifs of Mo were determined. Fourier transform (FT) in *R*-space of the $NiMoO_4/MoS_2/Ni_3S_2$/NF-1.7 and control samples of MoS_2 (Mo-S) and MoO_3 (Mo-O_I and Mo-O_{II}) are shown in Fig. 2C. In comparison to MoS_2 (Fig. 2C-a) and MoO_3 (Fig. 2C-b), chemical bonds of Mo-S, Mo-O, and Mo-Mo are observed in the $NiMoO_4/MoS_2/Ni_3S_2$/NF-1.7 (Fig. 2C-c), further proving the presence of the $NiMoO_4$ and MoS_2 phases.

The morphologies of the composites of $NiMoO_4/MoS_2/Ni_3S_2$/NF-*n* and control samples of $NiMoO_4$/NF and Ni_3S_2/NF were observed via scanning electron microscopy (SEM). For $NiMoO_4$/NF (Figs. S3a_1-a_3), thin nanosheets are observed to be distributed across the NF surface. For the sample of Ni_3S_2/NF, as shown in Figs. S3b_1-b_3, the entire NF surface is uniformly coated with bulky blocks of Ni_3S_2. After introducing both Mo and S sources, the resulting $NiMoO_4/MoS_2/Ni_3S_2$/NF-*n* exhibit microspheres (200–500 nm in diameter) filled with 3D cross-linked nanosheets (Fig. 3). The distribution of nanosheets on spheres would increase the specific surface area of the catalyst and promote its interaction with electrolytes, thereby facilitating the electrocatalysis. As shown in Fig. 3b_1-b_3, the morphology of $NiMoO_4/MoS_2/Ni_3S_2$/NF-1.7 is more regular, featuring distinctly separated nanosheets, which promote sufficient contact between the active sites and the electrolytes. At a lower S source dosage, such as $NiMoO_4/MoS_2/Ni_3S_2$/NF-1.3 (Fig. 3a_1-a_3), the nanosheets grown on material surface appear to be inadequate, leading to a reduced number of active sites. At the higher sulfur source, the $NiMoO_4/MoS_2/Ni_3S_2$/NF-2.0 sample (Fig. 3c_1-c_3) presents irregular spheres composed of clustered nanosheets, which may cover the exposed active sites. Hence, both excessive and insufficient addition of S source would negatively affect the morphology, with an optimal amount of 2 mmol. Elemental mapping (Fig. 3d_1-d_4) shows the S, O, Ni, and Mo on the surface of the $NiMoO_4/MoS_2/Ni_3S_2$/NF-1.7 are uniformly distributed, and energy dispersive spectroscopy (EDS) indicates the presence of these elements (see Fig. 3e). Notably, the signal of Ni element is notably weak in the elemental mapping, which suggests that the Ni-containing phase on material surface is primarily $NiMoO_4$, and the phases with high Ni contents including the Ni_3S_2 and Ni^0 (NF) would locate in the inner layer of the material. The dense distribution of the elements of Mo and S show the high content of the MoS_2 phase. Furthermore, the low distribution of O element confirms the less amount of $NiMoO_4$ than MoS_2, which is in good agreement to the high molar ratio of MoS_2 to $NiMoO_4$ in XANES.

Transmission electron microscopy (TEM) of $NiMoO_4/MoS_2/Ni_3S_2$/NF-1.7 shows that thin nanosheets are grown on the spheres (Fig. 4a, b). High-resolution TEM (HRTEM) images of red square regions in Fig. 4b are shown in Fig. 4c, d. there are only lattices of 0.23 (Fig. 4c) and 0.18 nm (Fig. 4d) observed, corresponding to (021) and (211) crystal planes of Ni_3S_2, respectively. This indicates that the two phases of $NiMoO_4$ and MoS_2 may exist in amorphous state or low crystallinity. Notably, the interfaces between Ni_3S_2 and amorphous/low-crystalline phases are observable, providing interactions for improving the electrocatalytic performance discussed below.

3.2. HER performance in acidic media

In 0.5 M H_2SO_4, the HER performance of $NiMoO_4/MoS_2/Ni_3S_2$/NF-*n*, $NiMoO_4$/NF, Ni_3S_2/NF, and Pt-C/NF was investigated. As shown in Fig. 5a, b and Table S2, the $NiMoO_4/MoS_2/Ni_3S_2$/NF-1.7 shows a η_{10} of 72 mV, which is much smaller than the $NiMoO_4/MoS_2/Ni_3S_2$/NF-1.3 (η_{10} = 128 mV) and $NiMoO_4/MoS_2/Ni_3S_2$/NF-2.0 (η_{10} = 131 mV). This

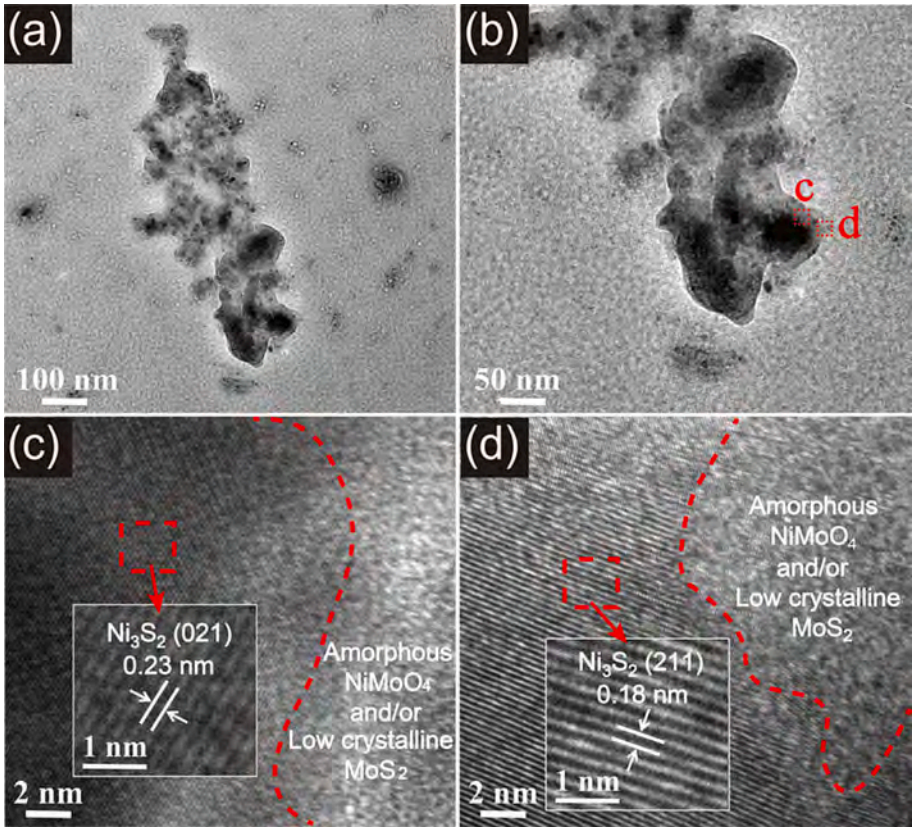

Fig. 4. (a, b) TEM and (c, d) HRTEM images of $NiMoO_4/MoS_2/Ni_3S_2$/NF-1.7.

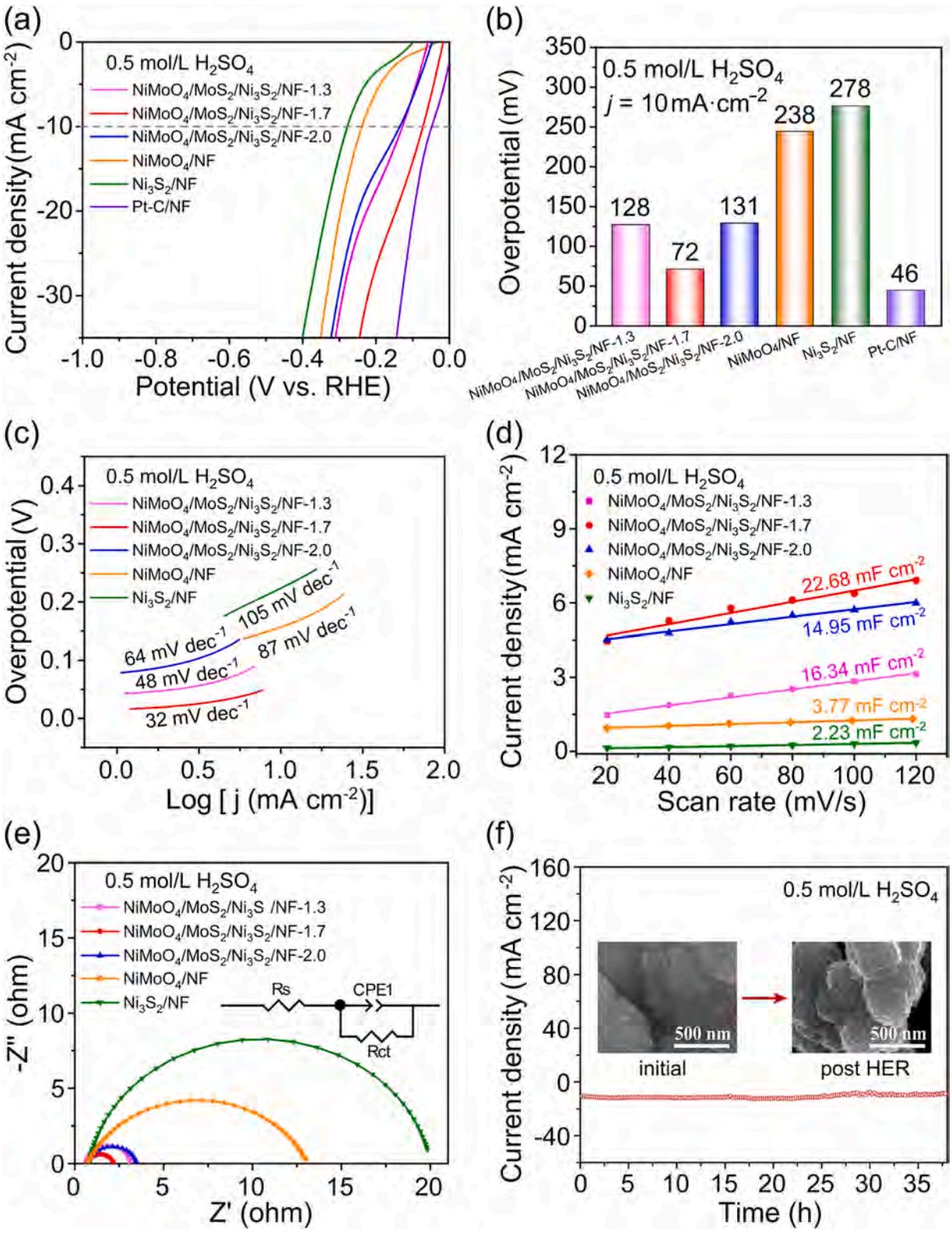

Fig. 5. (a) Polarization curves and (b) overpotentials of $NiMoO_4/MoS_2/Ni_3S_2$/NF-1.3, $NiMoO_4/MoS_2/Ni_3S_2$/NF-1.7, $NiMoO_4/MoS_2/Ni_3S_2$/NF-2.0, $NiMoO_4$/NF, Ni_3S_2/NF, and Pt-C/NF; (c) Tafel slopes, (d) electrochemical double-layer capcitance (C_{dl}), and (e) the fitting Nyquist plots of $NiMoO_4/MoS_2/Ni_3S_2$/NF-1.3, $NiMoO_4/MoS_2/Ni_3S_2$/NF-1.7, $NiMoO_4/MoS_2/Ni_3S_2$/NF-2.0, $NiMoO_4$/NF, and Ni_3S_2/NF; (f) chronoamperometric curve of $NiMoO_4/MoS_2/Ni_3S_2$/NF-1.7 at the constant overpotential of 183 mV and SEM images of the initial $NiMoO_4/MoS_2/Ni_3S_2$/NF-1.7 and post acidic HER sample. The electrolyte is 0.5 M H_2SO_4.

indicates that suitable S dosage benefits to the formation of nanosheets morphology with ample active sites. Compared with $NiMoO_4$/NF (η_{10} = 238 mV) and Ni_3S_2/NF (η_{10} = 278 mV), the η_{10} of $NiMoO_4/MoS_2/Ni_3S_2$/NF-1.7 is significantly reduced, suggesting interfacial interactions of the including phases in the composite effectively promote the HER activity. Table 1 lists a detailed comparison about HER performance of the known electrocatalysts [15,33,38,39,67–75]. As shown, the $NiMoO_4/MoS_2/Ni_3S_2$/NF-1.7 exhibits superior HER activity than the reported catalysts, such as $MoS_2/Co_9S_8/Ni_3S_2$/Ni (η_{10} = 103 mV) [15] and MoS_2/Ni_3S_2/NF (η_{10} = 176 mV) [15] supported by NF substrate, as well as NF-free materials, for instance, MoS_2/CoS_2 (η_{10} = 126 mV) [67], MoS_2/rGO/NiS (η_{10} = 152 mV) [70], Co_9S_8/NC@MoS_2 (η_{10} = 117 mV) [71], and the noble-metal based Ru@2H-MoS_2 (η_{10} = 168 mV) [68]. Compared with C-Co_2P@P-$NiMoO_4$/NF (η_{10} = 37 mV) [39], the HER activity of the $NiMoO_4/MoS_2/Ni_3S_2$/NF-1.7 is relatively inferior, while its facile synthetic method is more advantageous in mass production.

Tafel slopes are normally used to estimate HER kinetics and determine rate-determining step (RDS). In acidic solutions, HER process generally undergoes two steps: (1) in the first step, hydrated H^+ (H_3O^+) transfers to catalyst's surface and accepts one electron to yield an adsorbed hydrogen (H*) (Volmer step); (2) the second step involves two cases: (i) if H* is inadequate, another H^+ will adsorb on catalyst surface and accept another electron to generate an additional H*, afterwards, the two H* atoms would bind together to produce one H_2 molecule (Heyrovsky step); (ii) if the numbers of H* are sufficient, adjacent H* atoms will bind directly to generate and release H_2 (Tafel step) [25]. For the Volmer, Heyrovsky, and Tafel steps, the Tafel slopes would correspond to the values of 118, 39, and 30 mV·dec^{-1}, respectively [25,76].

Table 1
Comparison of HER performance of $NiMoO_4/MoS_2/Ni_3S_2$/NF with the reported electrocatalysts.

Catalysts	η_{10} (mV) and stability time			References
	0.5 M H_2SO_4	1 M KOH	1 M PBS	
$NiMoO_4/MoS_2/Ni_3S_2$/NF	**72 (38 h)**	**49 (200 h)**	**166 (200 h)**	**This work**
C-Co_2P@P-$NiMoO_4$/NF	37 (10 h)	59 (20 h)	50 (12 h)	J. Colloid Interf. Sci. 2023. [39]
$MoS_2/Co_9S_8/Ni_3S_2$/Ni	103 (80 min)	113 (24 h)	117 (20 h)	J. Am. Chem. Soc. 2019. [15]
MoS_2/Ni_3S_2/NF	176	203	279	J. Am. Chem. Soc. 2019. [15]
MoS_2/CoS_2	126 (10 h)	97 (10 h)	196 (10 h)	ACS Appl. Energy Mater. 2019. [67]
Ru@2H-MoS_2	168 (12 h)	51 (12 h)	137 (12 h)	Appl. Catal. B Environ. 2021. [68]
MoO_2/MoS_2/C	77 (20 h)	91 (20 h)	97 (20 h)	Adv. Funct. Mater. 2021. [69]
MoS_2/rGO/NiS	152 (10 h)	169 (10 h)	209 (10 h)	Nanomaterials 2021. [70]
Co_9S_8/NC@MoS_2	117 (12 h)	67 (12 h)	261 (12 h)	ACS Appl. Mater. Interfaces 2017. [71]
$NiMoS_3$	212 (10 h)	126 (10 h)	—	ACS Sustainable Chem. Eng. 2017. [72]
amorphous Ni_2P/crystalline P-$NiMoO_4$/amorphous P-$NiMoO_4$	—	45 (100 h)	—	ACS Nano 2024. [38]
NF/$NiMoO_4$@HeBiMoNi	—	53 (7.5 h)	—	Int. J. Hydrogen Energy 2024. [33]
N-$NiMoO_4/NiS_2$	—	99 (50 h)	—	Adv. Funct. Mater. 2019. [73]
P-doped $NiMoO_4$	—	144 (12 h)	—	Ceram. Int. 2021. [74]
$NiMoO_4$@$CoMoO_4$·xH_2O/NF	—	220 (24 h)	—	Small 2023. [75]

The Tafel slopes can be obtained from linear sweep voltammetry (LSV) curves. As displayed in Fig. 5c, the $NiMoO_4/MoS_2/Ni_3S_2$/NF-1.3, $NiMoO_4/MoS_2/Ni_3S_2$/NF-1.7, $NiMoO_4/MoS_2/Ni_3S_2$/NF-2.0, $NiMoO_4$/NF, and Ni_3S_2/NF show the Tafel slopes of 48, 32, 64, 87, and 105 mV·dec^{-1}, respectively. The smallest Tafel slope of the $NiMoO_4/MoS_2/Ni_3S_2$/NF-1.7 means it has the fastest electron transport rate. Also, the slope of 32 mV·dec^{-1} is very close to the value of 30 mV·dec^{-1}, suggesting the HER process in acidic media obeys Volmer-Tafel mechanism with Tafel step as the RDS.

The electrochemical active surface area (ECSA) is a critical parameter for evaluating exposure degree of the active sites. ECSA is proportional to the double-layer capacitance (C_{dl}), so we measured C_{dl} via cyclic voltammetry (CV, Figs. S4-S6). From Fig. 5d, the C_{dl} values follow an order of $NiMoO_4/MoS_2/Ni_3S_2$/NF-1.7 (22.68 mF·cm^{-2}) > $NiMoO_4/MoS_2/Ni_3S_2$/NF-1.3 (16.34 mF·cm^{-2}) > $NiMoO_4/MoS_2/Ni_3S_2$/NF-2.0 (14.95 mF·cm^{-2}) > $NiMoO_4$/NF (3.77 mF·cm^{-2}) > Ni_3S_2/NF (2.23 mF·cm^{-2}). The highest C_{dl} of the $NiMoO_4/MoS_2/Ni_3S_2$/NF-1.7 suggests it has the largest ECSA, with the maximum exposure of active sites.

Electrochemical impedance spectroscopy (EIS) was tested to investigate the electron transfer kinetics, and corresponding Nyquist diagrams were analyzed by Randall's equivalent circuit models. As seen from Fig. 5e and Table S3, the $NiMoO_4/MoS_2/Ni_3S_2$/NF-1.7 demonstrates a much lower charge transfer resistance (R_{ct} = 1.57 Ω) than other samples, indicating the fastest charge-transfer kinetics.

For practical applicability, operating stability of the electrocatalysts is pivotal. The stability testing of $NiMoO_4/MoS_2/Ni_3S_2$/NF-1.7 was performed at a settled overpotential of 183 mV. As found in Fig. 5f, the material may catalyze the HER at 10 mA·cm^{-2} for 38 h without any noticeable change, indicating an acceptable durability in the acidic solution. The durability time, as presented in Table 1, is much longer than that of most reported catalysts, particularly the NF-based materials without $NiMoO_4$ phase, such as the $MoS_2/Co_9S_8/Ni_3S_2$/Ni (stability time ~ 80 min) [15], suggesting the $NiMoO_4$ phase plays a key role in improving the stability of the catalyst. Also, the durability time of $NiMoO_4/MoS_2/Ni_3S_2$/NF-1.7 exceeds that of C-Co_2P@P-$NiMoO_4$/NF (10 h) [39], indicating that the heterointerfaces among $NiMoO_4$, MoS_2, and Ni_3S_2 phases make significant contributions to its durability, which facilitates substantial hydrogen production.

3.3. HER performance in alkaline media

In 1 M KOH, the HER performance of $NiMoO_4/MoS_2/Ni_3S_2$/NF-*n*, $NiMoO_4$/NF, Ni_3S_2/NF, and Pt-C/NF was tested. From Fig. 6a, b and Table S2, the η_{10} of 49 mV of $NiMoO_4/MoS_2/Ni_3S_2$/NF-1.7 is much lower than those of $NiMoO_4/MoS_2/Ni_3S_2$/NF-1.3 (η_{10} = 65 mV), $NiMoO_4/MoS_2/Ni_3S_2$/NF-2.0 (η_{10} = 73 mV), and the control samples of $NiMoO_4$/NF (η_{10} = 213 mV) and Ni_3S_2/NF (η_{10} = 269 mV). This indicates the highest activity of $NiMoO_4/MoS_2/Ni_3S_2$/NF-1.7. More importantly, the HER activity of $NiMoO_4/MoS_2/Ni_3S_2$/NF-1.7 is even higher than the Pt-C/NF catalyst (η_{10} = 67 mV). For comprehensive comparison, we tried to synthesize MoS_2/Ni_3S_2/NF as a control sample. However, because different synthetic conditions may lead to different morphologies and compositions, we directly refer to the data in literature. The η_{10} values of the reported MoS_2/Ni_3S_2/NF ranged 90 ~ 200 mV, with the MoS_2 phases in crystalline (98 mV) [23], low crystalline (~ 180 mV) [14], and amorphous state (109 mV) [50]. As shown in Table 1, the HER activity (η_{10} = 49 mV) of $NiMoO_4/MoS_2/Ni_3S_2$/NF-1.7 precedes most reported catalysts, such as the MoS_2-containg materials of $MoS_2/Co_9S_8/Ni_3S_2$/Ni (η_{10} = 113 mV) [15], MoO_2/MoS_2/C (η_{10} = 91 mV) [69], and Ru@2H-MoS_2 (η_{10} = 51 mV) [68], as well as the $NiMoO_4$-including materials of C-Co_2P@P-$NiMoO_4$/NF (η_{10} = 59 mV) [39], NF/$NiMoO_4$@HeBiMoNi (η_{10} = 53 mV) [33], and N-$NiMoO_4/NiS_2$ (η_{10} = 99

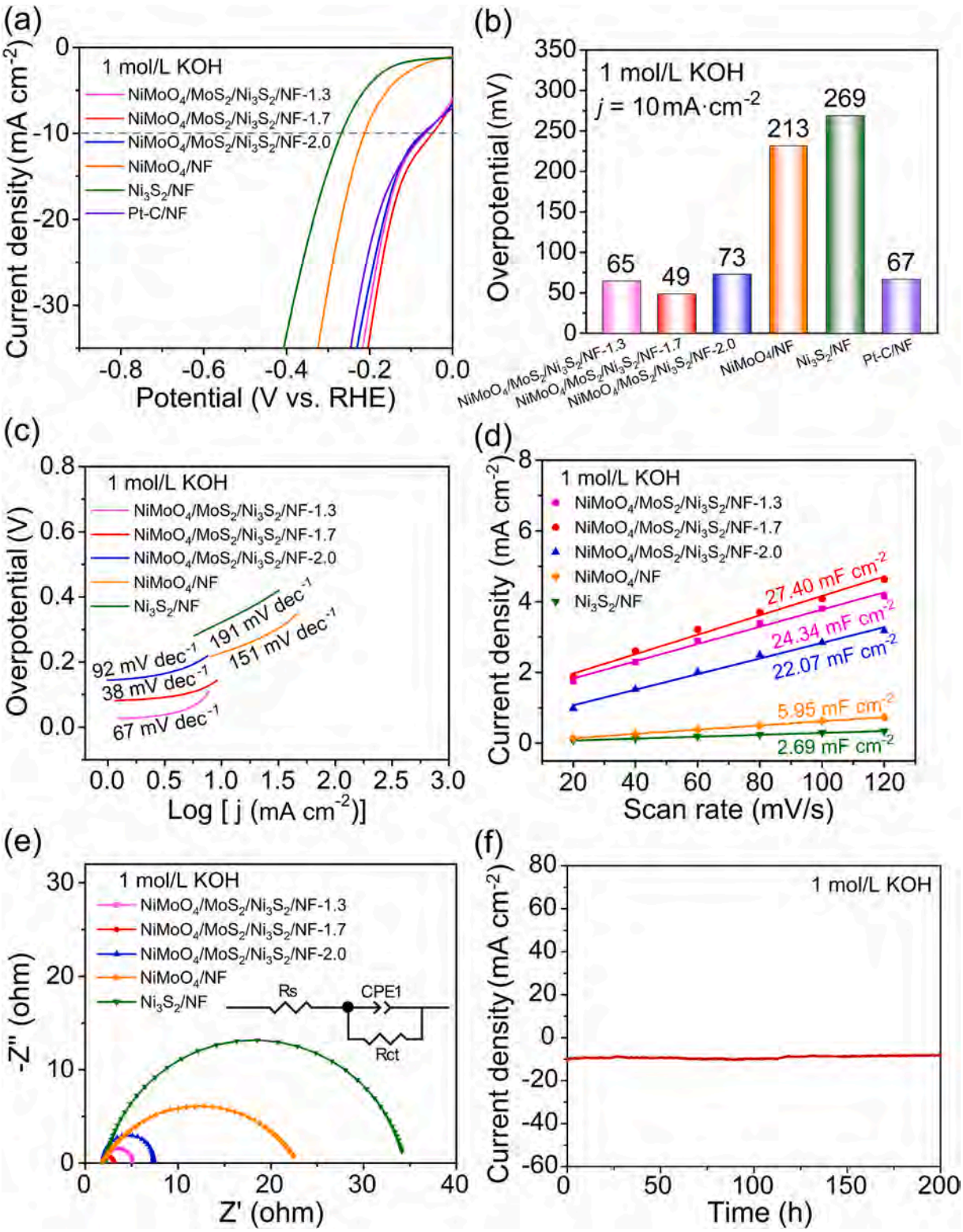

Fig. 6. (a) Polarization curves and (b) overpotentials of $NiMoO_4/MoS_2/Ni_3S_2$/NF-1.3, $NiMoO_4/MoS_2/Ni_3S_2$/NF-1.7, $NiMoO_4/MoS_2/Ni_3S_2$/NF-2.0, $NiMoO_4$/NF, Ni_3S_2/NF, and Pt-C/NF; (c) Tafel slopes, (d) electrochemical double-layer capacitance (C_{dl}), and (e) the fitting Nyquist plots of $NiMoO_4/MoS_2/Ni_3S_2$/NF-1.3, $NiMoO_4/MoS_2/Ni_3S_2$/NF-1.7, $NiMoO_4/MoS_2/Ni_3S_2$/NF-2.0, $NiMoO_4$/NF, and Ni_3S_2/NF; (f) chronoamperometric curve of $NiMoO_4/MoS_2/Ni_3S_2$/NF-1.7 at the constant overpotential of 133 mV. The electrolyte is 1 M KOH.

mV) [73,75]. Notably, the amorphous Ni_2P/crystalline P-$NiMoO_4$/amorphous P-$NiMoO_4$ [38] exhibited slightly lower η_{10} of 45 mV, while its synthesis involved two steps of hydrothermal reaction and high-temperature phosphorization, consuming more energy and needing long time.

HER kinetics in alkaline electrolytes is different from that in acidic ones, particularly regarding the water adsorption and dissociation. Detailed process can be described as: (1) one water molecule is initially

adsorbed on catalyst surface to form one H_2O^*, and due to the absence of H^+ in the system, the adsorbed H_2O^* molecules would take on the task of accepting the electron and dissociating to form H* and OH* (OH^- would release into the solution) (Volmer step); (2) if the as-generated H* is insufficient, another adsorbed H_2O is required to receive an electron to produce the additional H*, which binds to the preceding H* forming one H_2 (Heyrovsky step); (3) if the numbers of H* are enough (in this case, the adsorbed water molecules are adequate), they will direct bind to

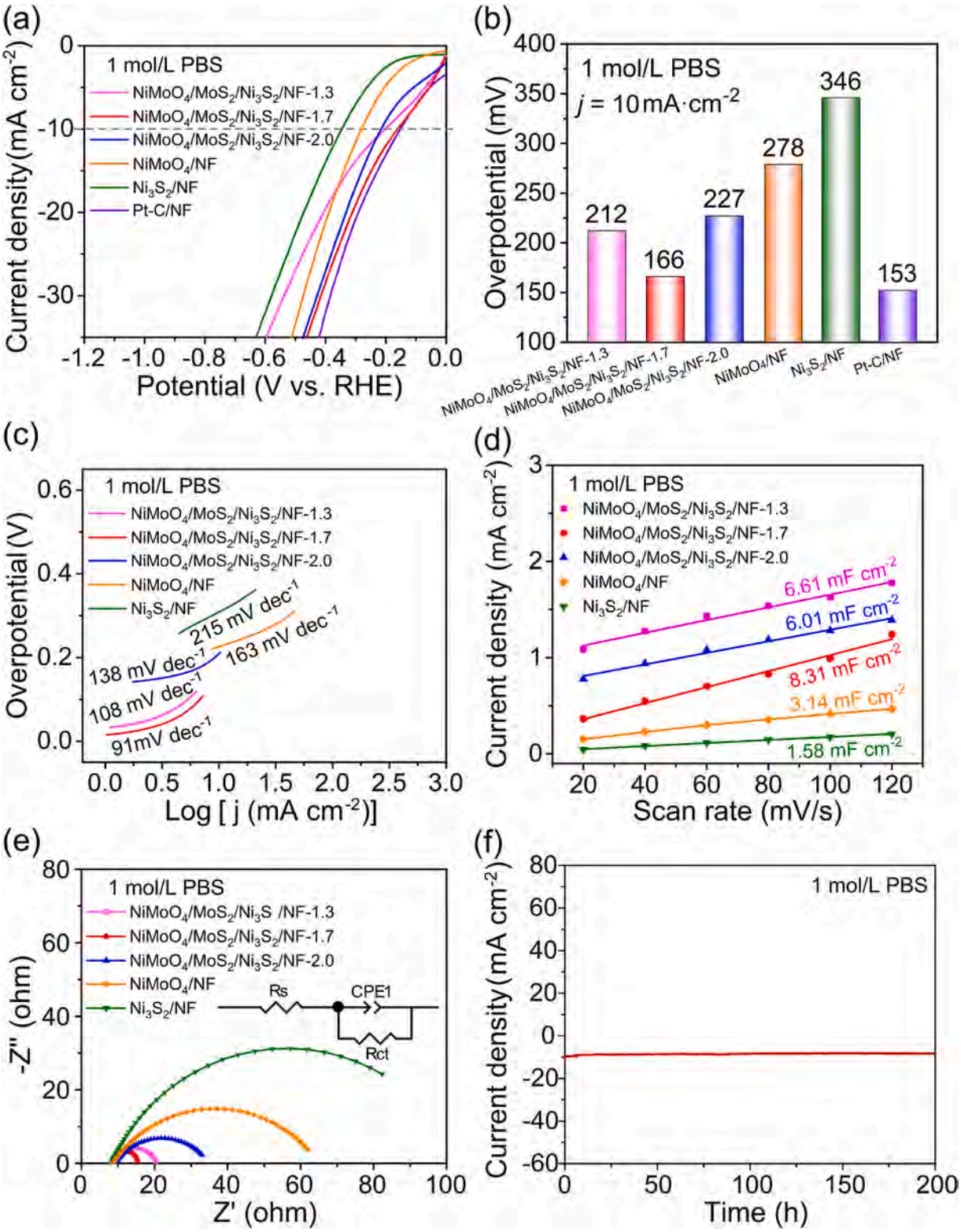

Fig. 7. (a) Polarization curves and (b) overpotentials of $NiMoO_4/MoS_2/Ni_3S_2$/NF-1.3, $NiMoO_4/MoS_2/Ni_3S_2$/NF-1.7, $NiMoO_4/MoS_2/Ni_3S_2$/NF-2.0, $NiMoO_4$/NF, Ni_3S_2/NF, and Pt-C/NF; (c) Tafel slopes, (d) electrochemical double-layer capacitance (C_{dl}), and (e) the fitting Nyquist plots of $NiMoO_4/MoS_2/Ni_3S_2$/NF-1.3, $NiMoO_4/MoS_2/Ni_3S_2$/NF-1.7, $NiMoO_4/MoS_2/Ni_3S_2$/NF-2.0, $NiMoO_4$/NF, and Ni_3S_2/NF; (f) chronoamperometric curve of $NiMoO_4/MoS_2/Ni_3S_2$/NF-1.7 at the constant overpotential of 249 mV. The electrolyte is 1 M PBS.

release the H_2 (Tafel step).

From Fig. 6c, Tafel slopes of $NiMoO_4/MoS_2/Ni_3S_2$/NF-1.3, $NiMoO_4/MoS_2/Ni_3S_2$/NF-1.7, $NiMoO_4/MoS_2/Ni_3S_2$/NF-2.0, $NiMoO_4$/NF, and Ni_3S_2/NF are 67, 38, 92, 151, 191 mV·dec^{-1}, respectively. The $NiMoO_4/MoS_2/Ni_3S_2$/NF-1.7 shows an extremely small Tafel slope (38 mV·dec^{-1}), which is very close to the value of 39 mV·dec^{-1} [25,76], suggesting the HER in alkaline media obeys the Volmer-Heyrovsky mechanism with Heyrovsky step being the RDS. As shown in Fig. 6d, the C_{dl} of 27.40 mF·cm^{-2} for $NiMoO_4/MoS_2/Ni_3S_2$/NF-1.7 is larger than that of $NiMoO_4/MoS_2/Ni_3S_2$/NF-1.3 (24.34 mF·cm^{-2}), $NiMoO_4/MoS_2/Ni_3S_2$/NF-2.0 (22.07 mF·cm^{-2}), $NiMoO_4$/NF (5.95 mF·cm^{-2}), and Ni_3S_2/NF (2.69 mF·cm^{-2}). The largest ECSA of $NiMoO_4/MoS_2/Ni_3S_2$/NF-1.7 means its maximum number of active sites, which facilitate the enhancement of HER performance. From Fig. 6e and Table S3, the $NiMoO_4/MoS_2/Ni_3S_2$/NF-1.7 exhibits the smallest charge transfer resistance (R_{ct}) of 1.15 Ω, suggesting the superior charge transfer capability.

The stability of $NiMoO_4/MoS_2/Ni_3S_2$/NF-1.7 is studied via a chronoamperometric test at a constant overpotential of 133 mV. From the I-t curve in Fig. 6f, after 200 h of HER operation, no significant degradation is observed at 10 mA·cm^{-2}. The durability is superior to most of the electrocatalysts (Table 1), such as $MoS_2/Co_9S_8/Ni_3S_2$/Ni (24 h) [15], Ru@2H-MoS_2 (12 h) [68], and other $NiMoO_4$-based materials like C-Co_2P@P-$NiMoO_4$/NF (20 h) [39], NF/$NiMoO_4$@HeBiMoNi (7.5 h) [33], and $NiMoO_4$@$CoMoO_4$·xH_2O/NF (24 h) [75]. The in situ growth of $NiMoO_4$, MoS_2, and Ni_3S_2 on NF and the formed heterogeneous interfaces greatly enhance the stability, making the $NiMoO_4/MoS_2/Ni_3S_2$/NF-1.7 an exceptionally promising candidate for practical application.

3.4. HER performance in neutral media

Considering the application requirement of hydrogen production in natural water source such as river, lake, or seawater, HER performance of the catalysts in neutral media was carried out, using 1 M phosphate buffered solution (PBS) as the electrolyte. As shown in Fig. 7a, b and Table S2, the HER activity of $NiMoO_4/MoS_2/Ni_3S_2$/NF-1.7 (η_{10} = 166 mV) is comparable to Pt-C/NF (η_{10} = 153 mV), and is superior to $NiMoO_4/MoS_2/Ni_3S_2$/NF-1.3 (η_{10} = 212 mV), $NiMoO_4/MoS_2/Ni_3S_2$/NF-2.0 (η_{10} = 227 mV), $NiMoO_4$/NF (η_{10} = 278 mV), and Ni_3S_2/NF (η_{10} = 346 mV). As listed in Table 1, the activity of $NiMoO_4/MoS_2/Ni_3S_2$/NF-1.7 exceeds many reported catalysts, such as MoS_2/Ni_3S_2/NF (η_{10} = 279 mV) [15], MoS_2/CoS_2 (η_{10} = 196 mV) [67], MoS_2/rGO/NiS (η_{10} = 209 mV) [70], and Co_9S_8/NC@MoS_2 (η_{10} = 261 mV) [71]. Though the HER activity $NiMoO_4/MoS_2/Ni_3S_2$/NF-1.7 is not as good as C-Co_2P@P-$NiMoO_4$/NF (η_{10} = 50 mV) [39] and $MoS_2/Co_9S_8/Ni_3S_2$/Ni (η_{10} = 117 mV) [15], its simple synthesis makes it more suitable for industrial amplification.

As indicated in Fig. 7c, the $NiMoO_4/MoS_2/Ni_3S_2$/NF-1.7 shows the smallest Tafel slope of 91 mV·dec^{-1}, suggesting it has the fastest HER kinetics. From Fig. 7d, the C_{dl} of 8.31 mF·cm^{-2} of $NiMoO_4/MoS_2/Ni_3S_2$/NF-1.7 is larger than those of $NiMoO_4/MoS_2/Ni_3S_2$/NF-1.3 (6.61 mF·cm^{-2}), $NiMoO_4/MoS_2/Ni_3S_2$/NF-2.0 (6.01 mF·cm^{-2}), $NiMoO_4$/NF (3.14 mF·cm^{-2}), and Ni_3S_2/NF (1.58 mF·cm^{-2}). These confirm the active sites of $NiMoO_4/MoS_2/Ni_3S_2$/NF-1.7 can be sufficiently exposed. As presented in Fig. 7e and Table S3, the decreased R_{ct} (6.40 Ω) of $NiMoO_4/MoS_2/Ni_3S_2$/NF-1.7 indicates the charge transfer rate is faster during neutral HER. The I-t curve of continuous HER testing shows no obvious decay over 200 h at a constant overpotential of 249 mV (Fig. 7f), demonstrating distinguished stability in neutral environment. As seen from Table 1, the exceptional durability of $NiMoO_4/MoS_2/Ni_3S_2$/NF-1.7 surpasses most reported electrocatalysts, such as C-Co_2P@P-$NiMoO_4$/NF (12 h) [39], $MoS_2/Co_9S_8/Ni_3S_2$/Ni (20 h) [15], and Ru@2H-MoS_2 (12 h) [68]. The enhanced stability is highly advantageous for actual applications.

3.5. Characterization of the samples after stability testing

The catalysts materials after stability testing are characterized by XRD, SEM, Raman, and XPS to assess the change of structures and morphology. Notably, under acidic conditions, a new diffraction peak emerges at 2θ of 13.2° (Fig. 8A-b), corresponding to the β-$NiMoO_4$ phase (JCPDS No. 12–0348). The observed $NiMoO_4$ diffractions may be attributed to the partial dissolution of Ni_3S_2 in the acidic solution, leading to a relative increased amount of β-$NiMoO_4$ that can be detected by XRD. This further confirms the existence of $NiMoO_4$ in the prepared composite. The XRD patterns (Fig. 8A-c, d) depict no obvious change after 200 h of HER testing in both basic and neutral solutions, indicating the well-preserved structure of $NiMoO_4/MoS_2/Ni_3S_2$/NF-1.7. Slight variations in the surface of $NiMoO_4/MoS_2/Ni_3S_2$/NF-1.7 (Fig. 5f and Fig. S7) demonstrate its robust stability across a wide range of pH. Raman (Fig. 8B) and XPS spectra (Fig. 8C-F and Fig. S8) after the durability tests also show close resemblance to those of the initial sample, implying the stability of the structure and chemical state. Table 1 exhibits the exceptional durability of $NiMoO_4/MoS_2/Ni_3S_2$/NF-1.7, which surpasses most reported catalysts.

3.6. DFT calculations

DFT calculations can help identify active sites and provide insights for the enhancement of HER activity. As mentioned before, the $NiMoO_4$ and MoS_2 phases play significant roles in the improved HER activity. The ΔG_{H^*} of electrocatalysts correlates with the exchange current density [77] (or overpotential at a fixed current density), and can be taken as a descriptor for HER activity. Generally, for a catalyst, a positive value of ΔG_{H^*} indicates weak binding affinity for hydrogen, thus requiring energy to realize effective hydrogen adsorption; conversely, a negative ΔG_{H^*} indicates the hydrogen adsorption is relatively stronger, while the desorption is relatively difficult [78]. Thus, the much reduced absolute value of ΔG_{H^*} ($|\Delta G_{H^*}|$) would correspond to the much enhancement of HER activity of the catalyst [78,79]. For the $NiMoO_4/MoS_2/Ni_3S_2$/NF composite, since Ni_3S_2 mainly contributes to improving the conductivity of the catalyst, for simplicity, we conduct DFT calculations on the $NiMoO_4/MoS_2$ heterojunction to figure out the coupling interactions of the amorphous/low crystalline phases.

The $|\Delta G_{H^*}|$ is a key criterion used to evaluate HER activity in acidic media, we calculate the MoS_2, $NiMoO_4$, $NiMoO_4/MoS_2$ ($NiMoO_4$ as adsorption surface), and $MoS_2/NiMoO_4$ (MoS_2 as adsorption surface). The optimized slabs and those with the adsorbed H* intermediates are presented in Fig. 9a-d. For MoS_2 (Fig. 9a) and $MoS_2/NiMoO_4$ (Fig. 9d), H atoms are preferentially adsorbed on the S sites. Conversely, for the $NiMoO_4$ (Fig. 9b) and $NiMoO_4/MoS_2$ (Fig. 9c), H atoms tend to be adsorbed on the O sites in both cases. As depicted in Fig. 9e, the individual MoS_2 phase shows a ΔG_{H^*} value of 1.80 eV (on S site), which closely aligns with the reported value of 1.82 eV [80], indicating that MoS_2 has a high energy barrier for H adsorption. For the $NiMoO_4$ phase, the negative ΔG_{H^*} value of −0.88 eV on the O site suggests a low energy barrier for H adsorption, resulting in strong adsorption force and hindered desorption. In the heterojunctions, the ΔG_{H^*} of S site of $MoS_2/NiMoO_4$ is −0.35 eV, and that of the O site of $NiMoO_4/MoS_2$ is 0.16 eV. For S site, the ΔG_{H^*} changing from a positive value (in MoS_2) to a negative one (in $MoS_2/NiMoO_4$) implies that the heterojunction formation makes the H adsorption process easier (hydrogen desorption becomes the RDS). For O site, the ΔG_{H^*} change from negative (in $NiMoO_4$) to positive (in $NiMoO_4/MoS_2$) values, indicating H adsorption is the RDS after heterojunction formation and the MoS_2 phase can promote hydrogen desorption. The much decreased $|\Delta G_{H^*}|$ by the $NiMoO_4$ phase suggests it plays a leading role in promoting the electrocatalytic activity.

As discussed above, in alkaline electrolytes, HER involves the steps of water adsorption, water dissociation (to produce H*), and H_2 release, thus, both the ΔG_{H2O^*} and ΔG_{H^*} affect the HER activity [29,81]. For the

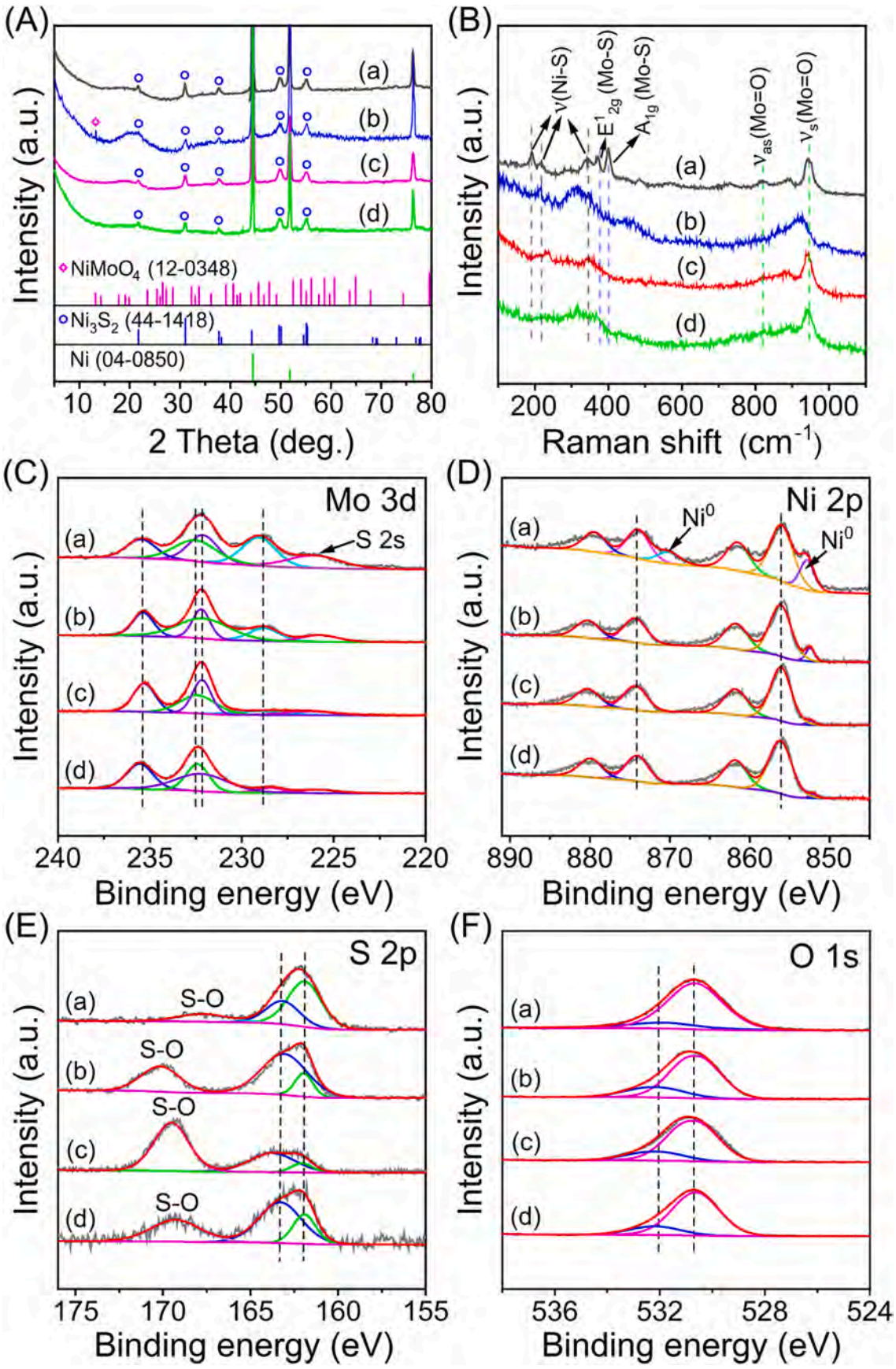

Fig. 8. (A) XRD patterns, (B) Raman, and XPS spectra ((C) Mo 3d, (D) Ni 2p, (E) S 2p, and (F) O 1 s) of (a) initial $NiMoO_4/MoS_2/Ni_3S_2$/NF-1.7, and after durability testing in (b) 0.5 M H_2SO_4 (38 h), (c) 1 M KOH (200 h), and (d) 1 M PBS (200 h).

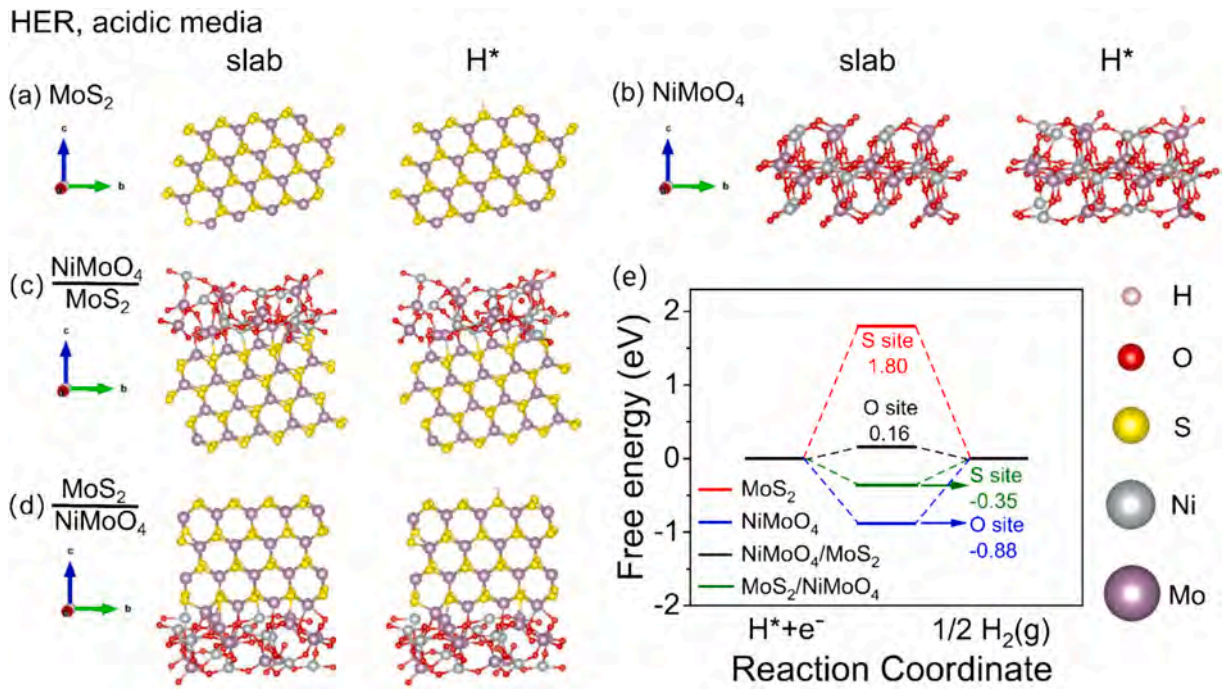

Fig. 9. Optimized structures at different reaction stages of (a) MoS_2, (b) $NiMoO_4$, (c) $NiMoO_4/MoS_2$, and (d) $MoS_2/NiMoO_4$; (f) Gibbs free energy for HER of MoS_2, $NiMoO_4$, $NiMoO_4/MoS_2$ and $MoS_2/NiMoO_4$ at U = 0 V and pH = 0. H: white, O: red, S: yellow, Ni: grey, Mo: purple. (For interpretation of the references to colour in this figure legend, the reader is referred to the web version of this article.)

more important step of water dissociation, it was found that the Ni site of $NiMoO_4$ contributed most prominently [29,38,82], thus in DFT calculations, we focus on the $NiMoO_4$ phase, so select the $NiMoO_4/MoS_2$ heterojunction (with $NiMoO_4$ as adsorption surface) and calculate the ΔG_{H2O^*} at the Ni site. For MoS_2, we calculate the ΔG_{H2O^*} at the Mo site which preferentially binds to H_2O. The binding sites for H atoms of the materials are consistent with those in acidic media, that is, S site of MoS_2 and O site of both $NiMoO_4$ and $NiMoO_4/MoS_2$.

Fig. 10a–c display the optimized structures of MoS_2, $NiMoO_4$, and $NiMoO_4/MoS_2$ slabs and those with the adsorbed intermediates (H_2O^*, OH^*+H^*, and H^*). As shown in Fig. 10d, the $NiMoO_4/MoS_2$ (Ni site) exhibits a lower ΔG_{H2O^*} of 0.68 eV than the individual phases of $NiMoO_4$ (0.96 eV, Ni site) and MoS_2 (1.13 eV, Mo site). This implies that the heterogeneous interface significantly promotes the water dissociation. Besides, the smallest $|\Delta G_{H^*}|$ of 0.65 eV (O site) of $NiMoO_4/MoS_2$ indicates the optimal HER activity, mainly benefiting from the facilitation of H* adsorption/desorption by the Ni-O species of $NiMoO_4$ [30]. These confirm that under alkaline conditions, the $NiMoO_4$ in the $NiMoO_4/MoS_2$ heterojunction contributes dominantly to the enhancement of HER activity. As described in the SEM-EDS mapping above, the components of $NiMoO_4$ and MoS_2, especially the $NiMoO_4$ would locate on the surface of the material, which ensures preferential contact with the electrolyte solutions and promotes the HER performance. Additionally, the synergistic interactions of Ni_3S_2 with a higher conductivity further help advance the electrocatalytic property.

Based on the above discussions, DFT calculations indicate that the O site in $NiMoO_4/MoS_2$ exhibits the most favorable ΔG_{H^*} in both acidic and alkaline electrolytes, and the Ni site is primarily responsible for water dissociation under alkaline condition. Hence, the $NiMoO_4$ plays a predominant role in facilitating the HER activity across a wide pH range. With the assistance of MoS_2, the $|\Delta G_{H^*}|$ value of O site in $NiMoO_4$ is significantly reduced and approaches the value of 0, highlighting the indispensable effect of MoS_2 in promoting hydrogen adsorption/desorption, thus augmenting HER activity. Effective interactions between $NiMoO_4$ and MoS_2 would contribute to the optimal catalytic performance.

Projected density of states (PDOS) are presented to investigate orbital hybridizations and further estimate the interaction strength through the analysis of the overlap among orbital peaks [46]. As presented in Fig. 10e, the PDOS curves of $NiMoO_4/MoS_2$-H reveals the hybridization between Ni-d, Mo-d, O-p, and H-s orbitals at the Fermi level (E_F, ~ 0 eV), indicating a robust interaction between the adsorbed H atom and the $NiMoO_4$ in $NiMoO_4/MoS_2$. The TDOS curves of MoS_2, $NiMoO_4$, and $NiMoO_4/MoS_2$, and $NiMoO_4/MoS_2$-H are displayed in Fig. 10f, g. The peak intensity at E_F for $NiMoO_4/MoS_2$ is higher than that of $NiMoO_4$ and MoS_2, suggesting an increased carrier density. This accelerates electron transfer, leading to enhanced activity at the interface of $NiMoO_4/MoS_2$ compared to the single phases of $NiMoO_4$ and MoS_2. Furthermore, after H adsorption, the TDOS peak intensity of $NiMoO_4/MoS_2$-H increases at E_F, meaning the electron transfer occurs between the $NiMoO_4/MoS_2$ interface and adsorbed H.

The electronic distribution at the $NiMoO_4/MoS_2$ heterojunction is analyzed via the calculated charge density difference (Fig. 11). The cyan regions depict a reduction in charge density, while the yellow regions signify an increase in charge density. From Fig. 11a, we can clearly observe the accumulation of electrons on O atoms and the loss of electrons on Mo atoms. Compared with the single-phase region far away from the interface, the electron density of O is much higher and the electron density of Mo is relatively lower in the interface area. This suggests that there exist electron transfers from Mo (in MoS_2) to O (in $NiMoO_4$) at the formed interface. The gain and loss of electrons can be quantitatively assessed through the plane-averaged charge density difference ($\Delta\rho$) along the Z-direction, where positive and negative peaks indicate regions of electron accumulation and depletion, respectively [83]. As shown in Fig. 11b, the interfacial $\Delta\rho$ values for $NiMoO_4/MoS_2$ are −0.8187 and 0.6380 e/Å^3, indicating that electrons are transferred from the low-layered MoS_2 to the upper-layered $NiMoO_4$. Notably, Fig. 11a also depicts sparse electron distribution (low electron density) of the Ni atom (in $NiMoO_4$) on the surface, which may enhance its affinity to electron-rich O atoms of H_2O, thereby promoting the water adsorption (and subsequent dissociation, an important process in alkaline HER). This is conducive to the enhancement of HER activity of the

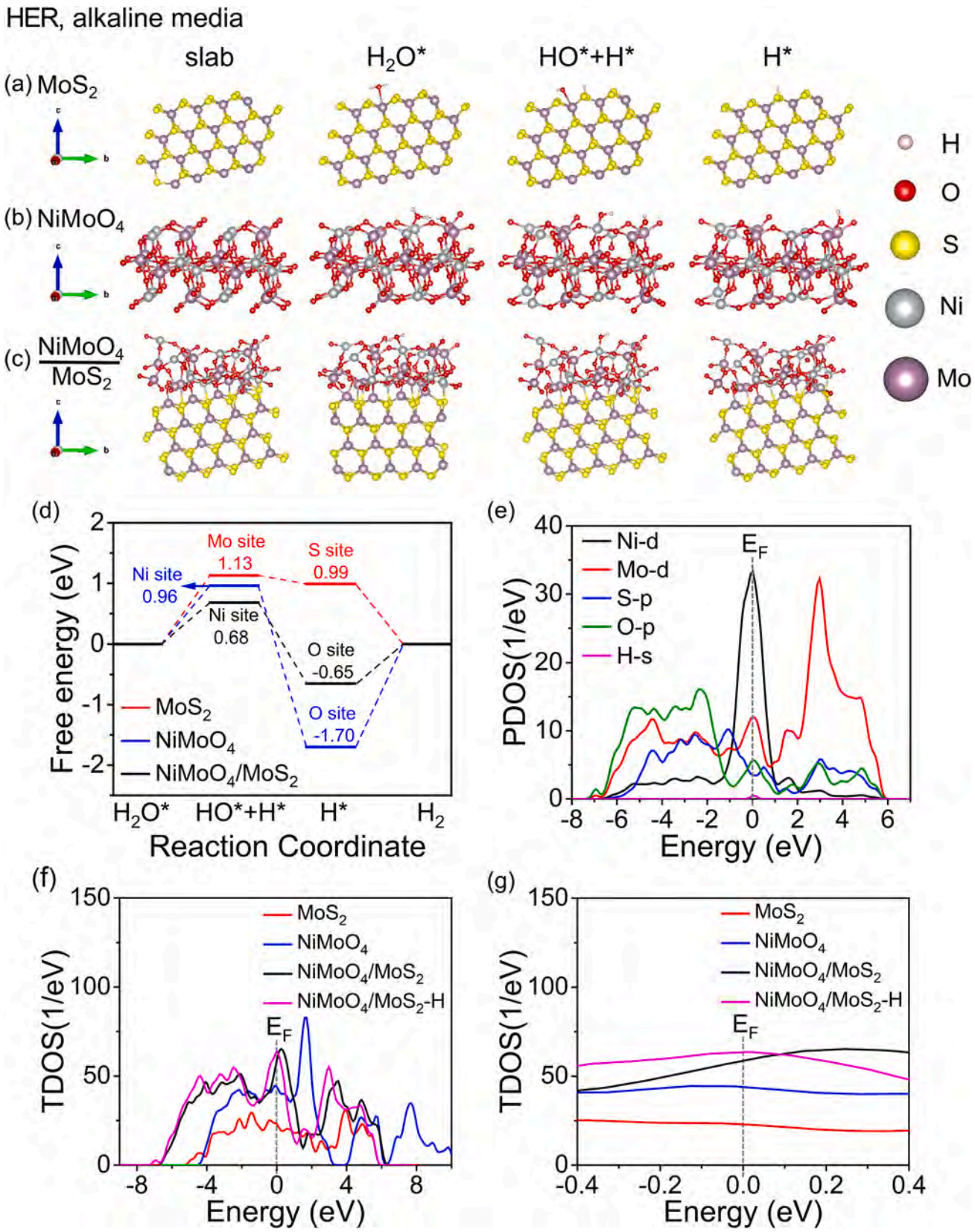

Fig. 10. Optimized structures at different reaction stages of (a) MoS_2, (b) $NiMoO_4$, and (c) $NiMoO_4/MoS_2$; (d) reaction energy diagram for H_2O dissociation and Gibbs free energy for HER of MoS_2, $NiMoO_4$ and $NiMoO_4/MoS_2$ at U = 0 V and pH = 13.8; (e) PDOS of H adsorption on $NiMoO_4/MoS_2$; (f, g) TDOS of MoS_2, $NiMoO_4$, $NiMoO_4/MoS_2$, and $NiMoO_4/MoS_2$ with H adsorption. (g) is the partial enlarged region of (f); H: white, O: red, S: yellow, Ni: grey, Mo: purple. (For interpretation of the references to colour in this figure legend, the reader is referred to the web version of this article.)

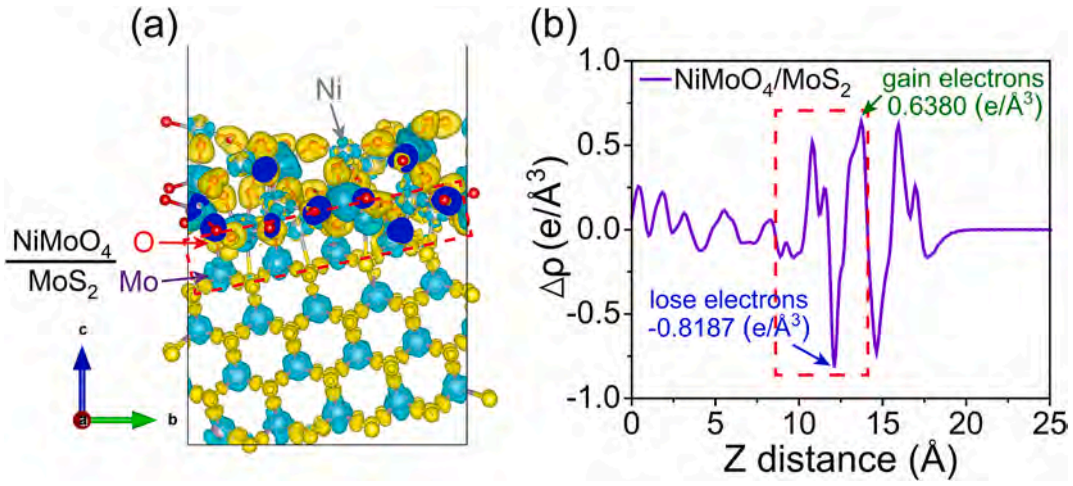

Fig. 11. (a) Charge density difference diagram of $NiMoO_4/MoS_2$ interface. The cyan regions signify a reduction in charge density, while the yellow regions denote an increase in charge density. (b) Plane-averaged charge density difference (Δρ) along Z-direction normal to the side views of $NiMoO_4/MoS_2$. O: red, S: yellow, Ni: grey, Mo: purple. (For interpretation of the references to colour in this figure legend, the reader is referred to the web version of this article.)

catalyst.

Drawing upon the above, primary benefits of the $NiMoO_4/MoS_2/Ni_3S_2$/NF-*n* in promoting HER performance are summarized as follows: (i) NF substrate and metallic Ni_3S_2 play pivotal roles in enhancing conductivity; (ii) the $NiMoO_4$ phase in $NiMoO_4/MoS_2$ significantly facilitates the HER activity in both acidic and alkaline electrolytes, particularly contributing to water dissociation under alkaline condition. (iii) MoS_2 phase in $NiMoO_4/MoS_2$ can promote hydrogen desorption in both acidic and alkaline media; (iv) synergistic interactions between $NiMoO_4$ and MoS_2 reduce H adsorption/desorption energy, resulting in an optimal $|\Delta G_{H^*}|$ and ΔG_{H2O^*}; (v) the heterogeneous interfaces of $NiMoO_4$, MoS_2, and Ni_3S_2 enrich the carrier density, improving the electrical conductivity of the catalysts.

4. Conclusion

In summary, via a simple one-pot hydrothermal reaction, we fabricate the $NiMoO_4/MoS_2/Ni_3S_2$/NF-*n* assembly integrating crystalline Ni_3S_2 with amorphous $NiMoO_4$ and low crystalline MoS_2 on 3D porous NF. The low reaction temperature (160 °C) and small S/Mo ratios (≤ 2) result in the low crystallinity of MoS_2 and the formation of $NiMoO_4$. The nanosheet morphology of well-engineered $NiMoO_4/MoS_2/Ni_3S_2$/NF-1.7 ensures the maximized exposure of electrocatalytic active sites, leading to superior HER performance. The in situ growth of $NiMoO_4$ and Ni_3S_2 on NF, and the formed heterointerfaces among the phases of $NiMoO_4$, MoS_2, and Ni_3S_2 promote the durability of the materials, which facilitates the large scale hydrogen production. DFT calculations demonstrate that in both acidic and alkaline electrolytes, the O site of $NiMoO_4$ in $NiMoO_4/MoS_2$ heterojunctions predominantly contributes to the boosted HER activity; more importantly, in alkaline electrolytes, the Ni site of $NiMoO_4$ facilitates the water dissociation. TDOS calculations reveal a higher carrier density due to interface interactions of the including phases, which is conducive to improving electrical conductivity of the catalysts. This work offers valuable guidance for designing novel hybrids of transitional metal sulfide/oxides to achieve exceptional HER performance over a wide pH range.

For future research endeavors, we propose to construct low-crystallinity multiphase composites by modulating reaction temperature via partial sulfidation or selenization. We aim to improve the electrocatalytic performance through the synergistic action between different phases, with a commitment to exploring electrocatalysts for overall water splitting. This work still has some drawbacks. If possible, future efforts will be made to investigate the heterojunctions of $NiMoO_4/MoS_2/Ni_3S_2$ using advanced characterization techniques such as scanning transmission electron microscopy (STEM). For a deeper understanding of the interactions of the contained phases and the influence of the formed interfaces on electrocatalytic performance, more heterojunctions including the Ni_3S_2 phase, such as the dual-phase heterojunction models of $NiMoO_4/Ni_3S_2$ and MoS_2/Ni_3S_2 and triple-phase heterojunction of $NiMoO_4/MoS_2/Ni_3S_2$, may be constructed for the DFT calculations.

CRediT authorship contribution statement

Senkai Han: Writing – original draft, Methodology, Investigation, Conceptualization. **Huiqin Yao:** Project administration, Funding acquisition. **Jiayi Zhan:** Validation, Methodology, Investigation. **Chaonan Wang:** Methodology, Investigation. **Siqi Zhang:** Investigation, Methodology. **Qingyang Gu:** Methodology, Funding acquisition. **Cheng Li:** Methodology, Investigation. **Shenghan Zhang:** Methodology, Investigation. **Hongliang Dong:** Methodology, Investigation. **Shulan Ma:** Writing – review & editing, Supervision, Funding acquisition, Conceptualization.

Declaration of competing interest

The authors declare that they have no known competing financial interests or personal relationships that could have appeared to influence the work reported in this paper.

Acknowledgments

This work is supported by the National Natural Science Foundation of China (No. 22176017), Natural Science Foundation of Ningxia (2023AAC02039), Natural Science Foundation of Beijing Municipality of China (2232051), Shanghai Key Laboratory of Material Frontiers Research in Extreme Environments (MFree) of China (No. 22dz2260800), and Shanghai Science and Technology Committee of China (No. 22JC1410300). We also thank the 1W2B beamline station at Beijing Synchrotron Radiation Facility (BSRF), the BL17B station of National Facility for Protein Science in Shanghai (NFPS) and BL13SSW station at Shanghai Synchrotron Radiation Facility (SSRF) of China.

Appendix A. Supplementary data

Supplementary data to this article can be found online at https://doi.org/10.1016/j.cej.2025.161095.

Data availability

Data will be made available on request.

References

[1] Z. Zeb, Y. Huang, L. Chen, W. Zhou, M. Liao, Y. Jiang, H. Li, L. Wang, L. Wang, H. Wang, T. Wei, D. Zang, Z. Fan, Y. Wei, Comprehensive overview of polyoxometalates for electrocatalytic hydrogen evolution reaction, Coord. Chem. Rev. 482 (2023) 215058.

[2] K. Bhunia, M. Chandra, S. Kumar Sharma, D. Pradhan, S.-J. Kim, A critical review on transition metal phosphide based catalyst for electrochemical hydrogen evolution reaction: Gibbs free energy, composition, stability, and true identity of active site, Coord. Chem. Rev. 478 (2023) 214956.

[3] M. Batool, A. Hameed, M.A. Nadeem, Recent developments on iron and nickel-based transition metal nitrides for overall water splitting: A critical review, Coord. Chem. Rev. 480 (2023) 215029.

[4] R. Boppella, J. Tan, J. Yun, S.V. Manorama, J. Moon, Anion-mediated transition metal electrocatalysts for efficient water electrolysis: Recent advances and future perspectives, Coord. Chem. Rev. 427 (2021) 213552.

[5] A.A. Mamun, A. Billah, M., Anisuzzaman Talukder, Effects of activation overpotential in photoelectrochemical cells considering electrical and optical configurations, Heliyon 9 (2023) e17191.

[6] J. Wang, Y. Gao, H. Kong, J. Kim, S. Choi, F. Ciucci, Y. Hao, S. Yang, Z. Shao, J. Lim, Non-precious-metal catalysts for alkaline water electrolysis: Operando characterizations, theoretical calculations, and recent advances, Chem. Soc. Rev. 49 (2020) 9154–9196.

[7] J. Kim, S.M. Jung, N. Lee, K.S. Kim, Y.T. Kim, J.K. Kim, Efficient alkaline hydrogen evolution reaction using superaerophobic Ni nanoarrays with accelerated H_2 bubble release, Adv. Mater. 35 (2023) 2305844.

[8] J. Lin, X. Wang, Z. Zhao, D. Chen, R. Liu, Z. Ye, B. Lu, Y. Hou, J. Lu, Design of pH-universal electrocatalysts for hydrogen evolution reaction, Carbon Energ. 6 (2024) e555.

[9] M. Wang, L. Zhang, Y. He, H. Zhu, Recent advances in transition-metal-sulfide-based bifunctional electrocatalysts for overall water splitting, J. Mater. Chem. A 9 (2021) 5320–5363.

[10] Y. Guo, T. Park, J.W. Yi, J. Henzie, J. Kim, Z. Wang, B. Jiang, Y. Bando, Y. Sugahara, J. Tang, Y. Yamauchi, Nanoarchitectonics for transition-metal-sulfide-based electrocatalysts for water splitting, Adv. Mater. 31 (2019) 1807134.

[11] L. Wang, X. Xue, Q. Luan, J. Guo, L. Chu, Z. Wang, B. Li, M. Yang, G. Wang, Interface engineering of Mo-doped Ni_9S_8/Ni_3S_2 multiphase heterostructure nanoflowers by one step synthesis for efficient overall water splitting, J. Colloid Interface Sci. 634 (2023) 563–574.

[12] N. Jiang, Q. Tang, M. Sheng, B. You, D.-E. Jiang, Y. Sun, Nickel sulfides for electrocatalytic hydrogen evolution under alkaline conditions: A case study of crystalline NiS, NiS_2, and Ni_3S_2 nanoparticles, Catal, Sci. Technol. 6 (2016) 1077–1084.

[13] Y. Chen, Y. Fan, Z. Cui, H. Huang, D. Cai, J. Zhang, Y. Zhou, M. Xu, R. Tong, Nickel sulfide-based electrocatalysts for overall water splitting, Int. J. Hydrogen Energ. 48 (2023) 27992–28017.

[14] Y. Miao, S. Yuan, H. Ren, A. Addad, A. Barras, P. Roussel, M.A. Amin, S. Szunerits, R. Boukherroub, Interface engineering of an ultrathin hierarchical phosphorus-doped MoS_2/Ni_3S_2 heterostructure on nickel foam for efficient water splitting, ACS Appl. Energy Mater. 6 (2023) 5856–5867.

[15] Y. Yang, H. Yao, Z. Yu, S.M. Islam, H. He, M. Yuan, Y. Yue, K. Xu, W. Hao, G. Sun, H. Li, S. Ma, P. Zapol, M.G. Kanatzidis, Hierarchical nanoassembly of $MoS_2/Co_9S_8/Ni_3S_2$/Ni as a highly efficient electrocatalyst for overall water splitting in a wide pH range, J. Am. Chem. Soc. 141 (2019) 10417–10430.

[16] Z. Yu, H. Yao, Y. Yang, M. Yuan, C. Li, H. He, T.-S. Chan, D. Yan, S. Ma, P. Zapol, M. G. Kanatzidis, MoO_xS_y/Ni_3S_2 microspheres on Ni foam as highly efficient, durable electrocatalysts for hydrogen evolution reaction, Chem. Mater. 34 (2022) 798–808.

[17] Z. Yu, H. Yan, C. Wang, Z. Wang, H. Yao, R. Liu, C. Li, S. Ma, Oxygen-deficient MoO_x/Ni_3S_2 heterostructure grown on nickel foam as efficient and durable self-supported electrocatalysts for hydrogen evolution reaction, Front. Chem. Sci. Eng. 17 (2023) 437–448.

[18] K.F. Mak, C. Lee, J. Hone, J. Shan, T.F. Heinz, Atomically thin MoS_2: A new direct-gap semiconductor, Phys. Rev. Lett. 105 (2010) 136805.

[19] Q.-L. Lin, Z.-F. Qian, X.-Y. Dai, Y.-L. Sun, R.-H. Wang, Regulation of electronic structure of monolayer MoS_2 by pressure, Rare Met. 41 (2022) 1761–1770.

[20] J. Zhang, T. Wang, D. Pohl, B. Rellinghaus, R. Dong, S. Liu, X. Zhuang, X. Feng, Interface engineering of MoS_2/Ni_3S_2 heterostructures for highly enhanced electrochemical overall-water-splitting activity, Angew. Chem. Int. Ed. 55 (2016) 6702–6707.

[21] S. Niu, J. Cai, G. Wang, Two-dimensional MoS_2 for hydrogen evolution reaction catalysis: The electronic structure regulation, Nano Res. 14 (2020) 1985–2002.

[22] L. Lei, D. Huang, G. Zeng, M. Cheng, D. Jiang, C. Zhou, S. Chen, W. Wang, A fantastic two-dimensional MoS_2 material based on the inert basal planes activation: Electronic structure, synthesis strategies, catalytic active sites, catalytic and electronics properties, Coord. Chem. Rev. 399 (2019) 213020.

[23] Y. Yang, K. Zhang, H. Lin, X. Li, H.C. Chan, L. Yang, Q. Gao, MoS_2-Ni_3S_2 Heteronanorods as efficient and stable bifunctional electrocatalysts for overall water splitting, ACS Catal. 7 (2017) 2357–2366.

[24] Y. Zhu, Q. Lin, Y. Zhong, H.A. Tahini, Z. Shao, H. Wang, Metal oxide-based materials as an emerging family of hydrogen evolution electrocatalysts, Energ, Environ. Sci. 13 (2020) 3361–3392.

[25] L. Quan, H. Jiang, G. Mei, Y. Sun, B. You, Bifunctional electrocatalysts for overall and hybrid water splitting, Chem. Rev. 124 (2024) 3694–3812.

[26] Y. Chen, Y. Lee, W. Chu, J. Li, Trace Ru-tuned NiO/CNT electrocatalysts outperform benchmark Pt for alkaline hydrogen evolution with superior mass activity, Chem. Eng. J. 472 (2023) 144922.

[27] T. Xiong, B. Huang, J. Wei, X. Yao, R. Xiao, Z. Zhu, F. Yang, Y. Huang, H. Yang, M. S. Balogun, Unveiling the promotion of accelerated water dissociation kinetics on the hydrogen evolution catalysis of $NiMoO_4$ nanorods, J. Energy Chem. 67 (2022) 805–813.

[28] Z. Xiao, J. Wang, C. Liu, B. Wang, Q. Zhang, Z. Xu, M.T. Sarwar, A. Tang, H. Yang, In-situ surface structural reconstruction of $NiMoO_4$ for efficient overall water splitting, Appl. Surf. Sci. 602 (2022) 154314.

[29] Z. Wang, J. Chen, E. Song, N. Wang, J. Dong, X. Zhang, P.M. Ajayan, W. Yao, C. Wang, J. Liu, J. Shen, M. Ye, Manipulation on active electronic states of metastable phase beta-$NiMoO_4$ for large current density hydrogen evolution, Nat. Commun. 12 (2021) 5960.

[30] W. Yuan, Z. Cui, S. Zhu, Z. Li, S. Wu, Y. Liang, Structure engineering of electrodeposited NiMo films for highly efficient and durable seawater splitting, Electrochim. Acta 365 (2021) 137366.

[31] H. Hao, Y. Li, Y. Wu, Z. Wang, M. Yuan, J. Miao, Z. Lv, L. Xu, B. Wei, In-situ probing the rapid reconstruction of FeOOH-decorated $NiMoO_4$ nanowires with boosted oxygen evolution activity, Mater. Today Energy 23 (2022) 100887.

[32] Q. Wang, Y. Duan, Z. Huang, X. Xu, J. Shi, L. Lin, S. Han, R. Jia, S. Chang, D. Wu, Synergetic modulation of a hierarchical nanoflower-like $NiMoO_4/Ni(OH)_2$ composite toward efficient alkaline water oxidation, Mater. Chem. and Phys. 305 (2023) 127949.

[33] Z. Liu, Y. Zou, F. Xu, J. Zhang, L. Sun, C. Xiang, $NiMoO_4$@H–BiMoNi with nanorod cluster structure for an efficient hydrogen evolution reactions in electrocatalysts, Int. J. Hydrogen Energy 51 (2024) 993–1001.

[34] G. Solomon, M.G. Kohan, R. Mazzaro, M. Jugovac, P. Moras, V. Morandi, I. Concina, A. Vomiero, MoS_2 nanosheets uniformly anchored on $NiMoO_4$ nanorods, a highly active hierarchical nanostructure catalyst for oxygen evolution reaction and pseudo-capacitors, Adv. Sustain. Syst. 7 (2022) 2200410.

[35] S.H. Yu, P.K. Gogoi, A. Rath, H. Dai, Z.Q. Cavin Ng, K. Suenaga, S.J. Pennycook, D. H.C. Chua, In-situ derived highly active NiS_2 and MoS_2 nanosheets on $NiMoO_4$ microcuboids via controlled surface sulfidation for high-current-density hydrogen evolution reaction, Electrochim. Acta 389 (2021) 138733.

[36] N. Xu, F.-L. Wang, C.-R. Li, J.-Y. Lv, X.-J. Zhai, W.-J. Li, Y.-L. Zhou, Y.-M. Chai, B. Dong, Constructing partially amorphous NiMoB/$NiMoO_4$-x with borate doping and reduction through one step boosting hydrogen evolution, J. Alloys Compd. 973 (2024) 172857.

[37] Y. Zhou, H.J. Fan, Progress and challenge of amorphous catalysts for electrochemical water splitting, ACS Mater. Lett. 3 (2020) 136–147.

[38] K. Zhang, Q. Su, W. Shi, Y. Lv, R. Zhu, Z. Wang, W. Zhao, M. Zhang, S. Ding, S. Ma, G. Du, B. Xu, Copious dislocations defect in amorphous/crystalline/amorphous sandwiched structure p-$NiMoO_4$ electrocatalyst toward enhanced hydrogen evolution reaction, ACS Nano 18 (2024) 3791–3800.

[39] D. Feng, X.Y. Liu, R. Ye, W. Huang, Y. Tong, Carbon-encapsulated Co_2P/P-modified $NiMoO_4$ hierarchical heterojunction as superior pH-universal electrocatalyst for hydrogen production, J. Colloid Interface Sci. 634 (2023) 693–702.

[40] P.E. Blochl, Projector augmented-wave method, Phys. Rev. B Condens. Matter. 50 (1994) 17953–17979.

[41] G. Kresse, J. Furthmuller, Efficient iterative schemes for ab initio total-energy calculations using a plane-wave basis set, Phys. Rev. B Condens. Matter. 54 (1996) 11169–11186.

[42] K.B. John, P. Perdew, M. Ernzerhof, Generalized gradient approximation made simple, Phys. Rev. Lett. 77 (1996) 3865–3868.

[43] W. Kohn, L.J. Sham, Self-consistent equations including exchange and correlation effects, Phys. Rev. 140 (1965) A1133–A1138.

[44] H. Yan, R. Deng, S. Zhang, H. Yao, J. Duan, H. Bai, Y. Li, R. Liu, K. Shi, S. Ma, Cd doped Ni_3S_2 nanosheet arrays grown on nickel foam as highly efficient and robust bifunctional electrocatalysts for alkaline overall water splitting, J. Alloys Compd. 954 (2023) 170072.

[45] H. Yan, R. Deng, C. Wang, H. Yao, S. Guo, R. Liu, S. Ma, Amorphous Fe hydroxide nanoparticles embedded in Ni_3S_2 as high-efficiency and low-cost electrocatalysts for oxygen evolution reaction, Electrochim. Acta 427 (2022) 140889.

[46] C. Wang, H. Yao, J. Sun, T. Tong, Z. Ye, H. Dong, C. Li, S. Ma, Nanoscale assembly of $MoS_2/CoS_2/Ni_3S_2$ grown on Ni foam for synergistic capture of iodine, Chem. Eng. J. 493 (2024) 152514.

[47] B. Qiao, H. Yan, C. Wang, H. Yao, Z. Cai, K. Shi, R. Liu, S. Ma, Ni_xS_y/NF composites assembled by sulfidation of nickel foam (NF) for highly effective capture of iodine, Chem. Eng. J. 479 (2024) 147864.

[48] J. Cao, J. Zhou, Y. Zhang, Y. Wang, X. Liu, Dominating role of aligned MoS_2/Ni_3S_2 nanoarrays supported on three-dimensional Ni foam with hydrophilic interface for highly enhanced hydrogen evolution reaction, ACS Appl. Mater. Interfaces 10 (2018) 1752–1760.

[49] N. Zhang, J. Lei, J. Xie, H. Huang, Y. Yu, MoS_2/Ni_3S_2 nanorod arrays well-aligned on Ni foam: A 3D hierarchical efficient bifunctional catalytic electrode for overall water splitting, RSC Adv. 7 (2017) 46286–46296.

[50] Z. Zheng, T. Su, J. Shi, R. Tong, H. Xiao, Q. Zhang, Y. Zhang, Z. Wang, Q. Li, X. Wang, Boosting the electrocatalytic activity of amorphous molybdenum sulfide nanoflakes via nickel sulfide decoration, Nanoscale 11 (2019) 22971–22979.

[51] Y.-H. Choi, J. Cho, A.M. Lunsford, M. Al-Hashimi, L. Fang, S. Banerjee, Mapping the electrocatalytic activity of MoS_2 across its amorphous to crystalline transition, J. Mater. Chem. A 5 (2017) 5129–5141.
[52] H.T. Wang, Z.Y. Lu, D.S. Kong, J. Sun, T.M. Hymel, Y. Cui, Electrochemical tuning of MoS_2 nanoparticles on three-dimensional substrate for efficient hydrogen evolution, ACS Nano 8 (2014) 4940–4947.
[53] Z. Yu, C. Wang, S. Guo, H. Yao, Z. Liang, R. Liu, K. Shi, C. Li, S. Ma, Triangle nanowall arrays of ultrathin MoS_2 nanosheets vertically grown on Co-Fe bimetallic disulfide as highly efficient electrocatalysts for hydrogen evolution reaction, Electrochim. Acta 403 (2022) 139683.
[54] F. Wang, H. Wu, H. Sun, L. Ma, W. Shen, Y. Li, M. Zheng, Hierarchical MoS_2/Ni_3S_2 core-shell nanofibers for highly efficient and stable overall-water-splitting in alkaline media, Mater. Today, Energy 10 (2018) 214–221.
[55] X. Zhuo, W. Jiang, T. Yu, G. Qian, J. Chen, H. Yang, S. Yin, Crystalline-amorphous Ni_3S_2-$NiMoO_4$ heterostructure for durable urea electrolysis-assisted hydrogen production at high current density, ACS Appl. Mater. Interfaces 14 (2022) 46481–46490.
[56] B. Huang, J. Yuan, Y. Lu, Y. Zhao, X. Qian, H. Xu, G. He, H. Chen, Hollow nanospheres comprising amorphous $NiMoS_4$ and crystalline NiS_2 for all-solid-state supercapacitors, Chem. Eng. J. 436 (2022) 135231.
[57] K.R. Shrestha, S. Kandula, N.H. Kim, J.H. Lee, Core cation tuned $M_xCo_{3-x}S_4$@ $NiMoS_4$ [M = Ni, Mn, Zn] core-shell nanomaterials as advanced all solid-state asymmetric supercapacitor electrodes, Chem. Eng. J. 405 (2021) 127046.
[58] G. Wang, Y. Xu, H. Yue, R. Jin, S. Gao, $NiMoS_4$ nanocrystals anchored on N-doped carbon nanosheets as anode for high performance lithium ion batteries, J. Colloid Interface Sci. 561 (2020) 854–860.
[59] M. Wei, X. Wu, Y. Yao, S. Yu, R. Sun, C. Wong, Toward high micro-supercapacitive performance by constructing graphene-supported $NiMoS_4$ hybrid materials on 3D current collectors, ACS Sustain. Chem. Eng. 7 (2019) 19779–19786.
[60] H. Du, F. Ding, J. Zhao, X. Zhang, Y. Li, Y. Zhang, J. Li, X. Yang, K. Li, Y. Yang, Core-shell structured Ni_3S_2@VO_2 nanorods grown on nickel foam as battery-type materials for supercapacitors, Appl. Surf. Sci. 508 (2020) 144876.
[61] H. Liu, D. Ouyang, Q. Zhou, C. Feng, Successional heterostructure MoS_2-Ni_3S_2 nanospheres based on 3D nano-porous Ni: An efficient electrocatalyst for overall water splitting, J. Alloys Compd. 920 (2022) 165243.
[62] C. Li, Q. Chen, R. Zheng, J. Huan, J. Bai, L. Zhu, Y. Huang, X. Zhu, Y. Sun, Regulation of sulfur atoms in MoS_x by magneto-electrodeposition for hydrogen evolution reaction, Small 20 (2023) 2308729.
[63] R.N. Durr, P. Maltoni, H. Tian, B. Jousselme, L. Hammarstrom, T. Edvinsson, From $NiMoO_4$ to gamma-NiOOH: Detecting the active catalyst phase by time resolved in situ and operando Raman spectroscopy, ACS Nano 15 (2021) 13504–13515.
[64] G. Solomon, R. Mazzaro, S. You, M.M. Natile, V. Morandi, I. Concina, A. Vomiero, Ag_2S/MoS_2 nanocomposites anchored on reduced graphene oxide: Fast interfacial charge transfer for hydrogen evolution reaction, ACS Appl. Mater. Interfaces 11 (2019) 22380–22389.
[65] P.A. Bertrand, Surface-phonon dispersion of MoS_2, Phys. Rev. B 44 (1991) 5745–5749.
[66] X. Lu, M.I.B. Utama, X. Wang, W. Xu, W. Zhao, M.H.S. Owen, Q. Xiong, Gate-tunable resonant raman spectroscopy of bilayer MoS_2, Small 13 (2017) 1701039.
[67] N. Huang, Y. Ding, S. Yan, L. Yang, P. Sun, C. Huang, X. Sun, Ultrathin MoS_2 nanosheets vertically grown on CoS_2 acicular nanorod arrays: A synergistic three-dimensional shell/core heterostructure for high-efficiency hydrogen evolution at full pH, ACS Appl. Energy Mater. 2 (2019) 6751–6760.
[68] J. Wang, W. Fang, Y. Hu, Y. Zhang, J. Dang, Y. Wu, B. Chen, H. Zhao, Z. Li, Single atom Ru doping 2H-MoS_2 as highly efficient hydrogen evolution reaction electrocatalyst in a wide pH range, Appl. Catal. B Environ. 298 (2021) 120490.
[69] F. Gong, M. Liu, S. Ye, L. Gong, G. Zeng, L. Xu, X. Zhang, Y. Zhang, L. Zhou, S. Fang, J. Liu, All-pH stable sandwich-structured MoO_2/MoS_2/C hollow nanoreactors for enhanced electrochemical hydrogen evolution, Adv. Funct. Mater. 31 (2021) 2101715.
[70] G. Liu, K. Thummavichai, X. Lv, W. Chen, T. Lin, S. Tan, M. Zeng, Y. Chen, N. Wang, Y. Zhu, Defect-rich heterogeneous MoS_2/rGO/NiS nanocomposite for efficient pH-universal hydrogen evolution, Nanomaterials (basel) 11 (2021) 662.
[71] H. Li, X. Qian, C. Xu, S. Huang, C. Zhu, X. Jiang, L. Shao, L. Hou, Hierarchical porous Co_9S_8/nitrogen-doped carbon@MoS_2 polyhedrons as pH universal electrocatalysts for highly efficient hydrogen evolution reaction, ACS Appl. Mater. Interfaces 9 (2017) 28394–28405.
[72] J. Guo, X. Zhang, Y. Sun, L. Tang, X. Zhang, $NiMoS_3$ nanorods as pH-tolerant electrocatalyst for efficient hydrogen evolution, ACS Sustain. Chem. Eng. 5 (2017) 9006–9013.
[73] L. An, J. Feng, Y. Zhang, R. Wang, H. Liu, G.C. Wang, F. Cheng, P. Xi, Epitaxial heterogeneous interfaces on N-$NiMoO_4$/NiS_2 nanowires/nanosheets to boost hydrogen and oxygen production for overall water splitting, Adv. Funct. Mater. 29 (2019) 1805298.
[74] Y. Song, W. Sha, M. Song, P. Liu, J. Tian, H. Wei, X. Hao, B. Xu, J. Guo, J. Liang, Defect-engineered ultrathin $NiMoO_4$ nanomeshes as efficient and stable electrocatalysts for overall water splitting, Ceram. Int. 47 (2021) 19098–19105.
[75] S. Barik, G.P. Kharabe, R. Illathvalappil, C.P. Singh, F. Kanheerampockil, P. S. Walko, S.K. Bhat, R.N. Devi, C.P. Vinod, S. Krishnamurty, S. Kurungot, Active site engineering and theoretical aspects of "superhydrophilic" nanostructure array enabling efficient overall water electrolysis, Small 19 (2023) 2304143.
[76] X. Tian, P. Zhao, W. Sheng, Hydrogen evolution and oxidation: Mechanistic studies and material advances, Adv. Mater. 31 (2019) 1808066.
[77] J.K. Nørskov, T. Bligaard, A. Logadottir, J.R. Kitchin, J.G. Chen, S. Pandelov, U. Stimming, Trends in the exchange current for hydrogen evolution, J. Electrochem. Soc. 152 (2005) J23.
[78] X. Teng, Z. Wang, Y. Wu, Y. Zhang, B. Yuan, Y. Xu, R. Wang, A. Shan, Enhanced alkaline hydrogen evolution reaction of MoO_2/Ni_3S_2 nanorod arrays by interface engineering, Nano Energy 122 (2024) 109299.
[79] X. Yu, L. Qu, C. Lee, J. Peng, Q. Yan, H. Bai, M. Yao, Bismuth-nickel bimetal nanosheets with a porous structure for efficient hydrogen production in neutral and alkaline media, Nanoscale 14 (2022) 17210–17221.
[80] H. Zhao, Z. Li, J. Deng, X. Dai, M. Cui, F. Nie, X. Zhang, Z. Ren, Y. Wang, W. Song, J. Liu, Amorphous MoS_2 nanosheets on MoO_2 films/Mo foil as free-standing electrode for synergetic electrocatalytic hydrogen evolution reaction, Int. J. Hydrogen Energy 45 (2020) 17422–17433.
[81] J. Zhang, S. Zhang, X. Zhang, Z. Ma, Z. Wang, B. Zhao, Construction of Ni_4Mo/MoO_2 heterostructure on oxygen vacancy enriched $NiMoO_4$ nanorods as an efficient bifunctional electrocatalyst for overall water splitting, J. Colloid Interface Sci. 650 (2023) 1490–1499.
[82] G.L. Li, X.Y. Qiao, Y.Y. Miao, T.Y. Wang, F. Deng, Synergistic effect of N-$NiMoO_4$/Ni heterogeneous interface with oxygen vacancies in N-$NiMoO_4$/Ni/CNTs for superior overall water splitting, Small 19 (2023) 2207196.
[83] B. Qi, W. Chang, Q. Xu, L. Jiang, S. An, J.F. Chu, Y.F. Song, Regulating hollow carbon cage supported NiCo alloy nanoparticles for efficient electrocatalytic hydrogen evolution reaction, ACS Appl. Mater. Interfaces 15 (2023) 12078–12087.